Spatial and temporal heterogeneity of mouse and human microglia at single-cell resolution

Spatial and developmental heterogeneity of mouse and human microglia at single-cell resolution

Takahiro Masuda[1,14], Roman Sankowski[1,14], Ori Staszewski[1,14], Chotima Böttcher[2], Lukas Amann[1,15], Christian Scheiwe[3], Stefan Nessler [4], Patrik Kunz[4], Geert van Loo[5,6], Volker Arnd Coenen[7], Peter C. Reinacher[7], Anna Michel[8], Ulrich Sure[8], Ralf Gold[9], Josef Priller[2,10,11], Christine Stadelmann[4] & Marco Prinz[1,12,13]

[1]Institute of Neuropathology, Medical Faculty, University of Freiburg, Freiburg, Germany
[2]Department of Neuropsychiatry and Laboratory of Molecular Psychiatry, Charité – Universitätsmedizin Berlin, Berlin, Germany,
[3]Clinic for Neurosurgery, Faculty of Medicine, University of Freiburg, Freiburg, Germany
[4]Institute of Neuropathology, University Medical Center Göttingen, Göttingen, Germany
[5]VIB Center for Inflammation Research, Ghent, Belgium
[6]Department of Biomedical Molecular Biology, Ghent University, Ghent, Belgium
[7]Department of Stereotactic and Functional Neurosurgery, Medical Faculty, University of Freiburg, Freiburg, Germany
[8]Department of Neurosurgery, University Hospital Essen, Germany
[9]Department of Neurology, St. Josef-Hospital, Ruhr University Bochum, Bochum, Germany
[10]DZNE and BIH, Berlin, Germany
[11]University of Edinburgh and UK DRI, Edinburgh, UK
[12]BIOSS Centre for Biological Signalling Studies, University of Freiburg, Germany
[13]CIBSS Centre for Integrative Biological Signalling Studies, University of Freiburg, Germany
[14]These authors contributed equally to this work
[15]Faculty of Biology, University of Freiburg, Freiburg, Germany.

Correspondence to:
Marco Prinz, M.D.
Institute of Neuropathology
University of Freiburg
Breisacher Str. 64
D-79106 Freiburg, Germany
Phone: +49-761-270-51050
E-mail: marco.prinz@uniklinik-freiburg.de

ABSTRACT

Microglia play critical roles in neural development and homeostasis. They are also implicated in neurodegenerative and neuroinflammatory diseases of the central nervous system (CNS). However, little is known about the presence of spatially and temporally restricted subclasses of microglia during CNS development and disease. Here, we combined massively parallel single-cell analysis, single-molecule FISH, advanced immunohistochemistry and computational modelling to comprehensively characterize novel microglia subclasses in up to six different regions during development and disease. Single-cell analysis of mouse CNS tissues revealed specific time- and region-dependent microglia subtypes, which were transcriptionally distinct from perivascular macrophages, during homeostasis. Demyelinating and neurodegenerative diseases evoked context-dependent microglia subtypes with distinct molecular hallmarks and diverse cellular kinetics. Diverse microglia clusters were also identified in normal and diseased human brains. Our data provide new insights into the endogenous immune system of the CNS during development, health and disease.

Key words: microglia, perivascular macrophages, single-cell analysis, immune system, human, mouse

INTRODUCTION

Tissue-resident myeloid cells in the central nervous system (CNS) represent a heterogeneous class of innate immune cells that are essential for the maintenance of tissue homeostasis (*1*). Parenchymal microglia and the CNS-associated macrophages (CAMs), including leptomeningeal (mMΦ), perivascular (pvMΦ) and choroid plexus macrophages (cpMΦ), are the organ-specific macrophages of the CNS with pivotal roles in health and disease (*2-4*).

Despite of the similarities that microglia and CAMs share with various other tissue-resident macrophages, the parenchymal and non-parenchymal CNS macrophages have two distinctive properties, namely a restricted prenatal origin and a remarkable longevity (*4, 5*). It is now generally believed that microglia and CAMs are derived from early yolk sac erythromyeloid precursors in a *c-myb*- and chemokine receptor (CCR)2-independent fashion (*6-8*). These specific developmental pathways and anatomical niches make CNS-endogenous macrophages distinct from other tissue macrophages, such as those in the aorta, skin, heart, liver, spleen and other organs (*9-12*).

When compared to other hematopoietic cells, microglia and CAMs persist over a very long period of time with low but constant rates of self-renewal (*13, 14*) coupled to cell apoptosis (*15*). This longevity necessitates adaptivity of microglia towards environmental challenges (*16, 17*) and cell perturbations (*18*). Since microglia act as guardians of the CNS, continuously scavenging for dying cells, pathogens, and molecules through microbial-associated molecular pattern receptor-dependent and -independent mechanisms (*1*), these highly diverse and specialized functions may be executed by microglia subsets that already pre-exist *in situ*, or alternatively, by specific development of microglia subsets from a homogeneous pool of cells upon demand. To date, the spatiotemporal heterogeneity of microglia during development, homeostasis and disease has not been studied at the single-cell level.

Previous approaches used to analyse microglial diversity have largely relied on immunophenotyping by flow cytometry complemented with histological analysis of RNA and

proteins *in situ* (*19, 20*). More recently, comprehensive transcriptomic (*21*) and proteomic (*22*) profiling of bulk populations of large numbers of microglia helped to reveal microglial heterogeneity in the mouse brain. Indeed, different microglia states were identified during development (*7, 12, 23-25*), homeostasis (*26*) and disease (*27*). Although these approaches provided important insights, they have notable limitations. Earlier single-cell analyses of microglia, for instance via flow cytometry, *in situ* hybridization or immunohistochemistry, were limited to probing a few selected proteins or RNAs. Due to a bias toward candidate genes/proteins, these approaches allow neither analysis of comprehensive expression landscapes nor discovery of previously unrecognized molecules (*28*). In contrast, transcriptomic analysis of bulk preparations of microglial RNA may conceal the diversity of microglia across different brain regions by relying on ensemble averages (*21, 29, 30*).

During the last few years, the revolution in single-cell genomics has enabled an unbiased genome-wide quantification and multiplex spatial analysis of RNA in single microglia *in situ* as well as *in vitro* (*31*). However, recent single-cell RNA-sequencing (scRNA-seq) studies of microglia either only used pre-sorted myeloid cell populations (*32*), or whole brain approaches (*33*) without addressing the question of spatially and temporally restricted subtypes of microglia in several regions of the CNS. Importantly, single-microglia profiling data from humans is not yet available at all, although this knowledge may greatly improve our understanding of the pathogenesis of neuropsychiatric diseases.

By combining massively parallel scRNA-seq with single-molecule FISH (smFISH), advanced triple immunohistochemistry, high-resolution microscopy, and computational modelling, we were able to comprehensively characterize microglial diversity in different regions of the mouse and human brain during development and health. We identify molecules that characterize microglial populations involved in neuroinflammatory and neurodegenerative conditions in mice and humans, and highlight context- and time-dependent microglia subsets and their distinct signals. The data provide new potential therapeutic targets and a valuable resource for the study of disease mechanisms in the CNS.

RESULTS

Distinct cell-specific signatures of individual microglia and pvMΦ in the juvenile mouse brain

We first used an unbiased, surface marker-free approach to study the complexity of the CNS of prepubescent juvenile mice and to determine how transcriptionally dissimilar microglia and pvMΦ are as compared to the other CNS cells. For this purpose, we prepared a CNS cell suspension devoid of meninges and choroid plexus (**Fig. 1a**). We then performed quantitative scRNA-seq of 3,047 CNS cells as described before (*34*). Individual RNA molecules were counted using molecular identifiers (UMIs) as performed recently (*8, 34*), which greatly reduces PCR amplification bias.

Dimensionality reduction using *t*-distributed stochastic neighbor embedding (*t*-SNE) revealed that both microglia and pvMΦ were transcriptionally related, whereas neurons, oligodendrocytes, astrocytes, endothelial cells and vascular smooth muscle cells (VSMC) had a distinct RNA profile (**Fig. 1b**). In order to define the transcriptional differences that allow for the distinction of cell types in the CNS, we generated a heat map from 2,996 single sorted cells showing the 49 most variable genes (**Fig. 1c**). Microglia and pvMΦ shared some markers like *Aif1*, *Csf1r* and *Tyrobp* (**Extended Data Fig. 1a**), but microglia were distinguishable from pvMΦ and other CNS cells on the basis of their expression of *Tgfbr*, *Gpr34*, *Hexb*, *Selplg*, *Il1a* (**Fig. 1c**). In contrast, pvMΦ expressed higher mRNA levels of *Folr2*, *Lyve1*, *F13a1*, *Cbr2*, *Mrc1*, *Pf4*, *Cd163*, *Ccl24* and *Cd209f*. Gene ontology (GO) analysis comparing gene expression profiles of microglia and pvMΦ suggested functional involvement of microglia in cell chemotaxis, inflammatory response and regulation of cell adhesion, whereas pvMΦ were involved in inflammatory response, regulation of response to external stimulus, endocytosis and cytokine production (**Extended Data Figs. 1b, c**). Visualization of scRNA-seq data on *t*-SNE plots revealed that microglia and pvMΦ populations are distinguishable based on their transcriptomic signature (**Fig. 1d**). Taken

together, these data reveal that microglia and pvMΦ are transcriptionally distinct myeloid cell populations in the CNS.

Comprehensive transcriptome analysis microglia during development, homeostasis and disease by single-cell RNA-sequencing

Recent whole transcriptome analysis of microglia development from yolk sac progenitors to adult microglia highlighted the degree to which cells change during this interval, showing dramatic differences in microglial gene expression between early postnatal periods and adulthood (*7, 12, 25*). However, it is still unknown whether microglia subclasses with distinct transcriptional profiles emerge during development. In order to study microglia heterogeneity on single-cell level during different homeostatic conditions, we collected single microglia cells from multiple anatomical regions of the embryonic (embryonic day E16.5), juvenile (3 weeks) and adult (16 weeks) mouse CNS (**Fig. 2a**). The areas were selected to match those previously found to exhibit transcriptional differences of microglial bulk RNA on Affymetrix analysis (*21*). To further compare expression patterns during homeostasis to those under pathological conditions, microglia were also isolated from neurodegenerative (facial nerve axotomy) and demyelinating (cuprizone paradigm) disease models (**Fig. 2a**). In order to increase the yield, microglia were FACS-sorted from four different CNS regions during embryogenesis and up to six different CNS regions for postnatal time points (**Fig. 2a and Suppl. Fig. 1**). Following quality control, data from a total of 3,826 single microglia were further analyzed using the RaceID algorithm (Herman JS, 2018) and finally depicted in *t*-SNE plots (**Fig. 2b and Suppl. Fig. 2**). Unsupervised clustering gave rise to 13 distinct clusters, resembling ten microglia clusters during development (C1-C10) and one cluster for degeneration (C11) and two clusters for demyelination and remyelination (C12 and C13) (**Fig. 2c**).

Spatiotemporal specificity of the emergence of microglia subsets during development

To investigate microglia diversity during development, we first focused on microglia from non-diseased CNS regions. *t*-SNE plots visualized two main clouds that clearly segregate embryonic and postnatal microglia (**Fig. 3a**). Unbiased clustering of the top differentially regulated genes revealed the presence of ten major clusters of microglia (C1-10) with distinct transcriptional profiles (**Figs. 3b, c and Suppl. Fig. 3**). Among them, the C1-6 clusters predominantly consisted of embryonic microglia, whereas the postnatal microglia constituted C7-10 clusters (**Figs. 3a, b**). Notably, embryonic clusters (C1-6) were differently distributed across the four embryonic CNS regions tested (**Figs. 3d, e**). For instance, the C2 cluster was enriched in embryonic forebrain and midbrain, whereas the C6 microglia was predominantly observed in cerebellum and spinal cord (**Figs. 3d, e**). Likewise, the postnatal clusters showed a spatiotemporally variable distribution. For example, , e.g. the C10 cluster was enriched in juvenile cortical and hippocampal microglia (86.0 % and 71.7 % of microglia in the cortex and in the hippocampus, respectively, compared to 25.7 % in the cerebellum, **Figs. 3d, e**). Furthermore, the minor C7 cluster was more prevalent in cerebellum and corpus callosum during adulthood (for both regions 12.3 % and 8.9 % of microglia in the cerebellum and in the corpus callosum compared to 5.6 % in the cortex). The relative proportion of clusters in the cerebellum didn´t change between the juvenile and the adult stages, which is in sharp contrast to what was observed in the cortex and hippocampus, where the C10 microglia decreased at the expense of the C7 and C8 clusters in adulthood (**Figs. 3d, e**). Overall, adult microglia showed a more homogenous distribution of each cluster across regions than juvenile microglia (**Figs. 3d, e**). Together, these data suggest that microglia exhibit different subtypes with distinct gene expressional profiles over the course of development with strong variation between different CNS regions that might reflect local maturation differences.

Among the top differentially regulated genes during development were the microglial homeostatic genes *Tmem119*, *Selplg* and *Slc2a5*, which were highly induced at postnatal stages (**Fig. 4a**). In addition, expression of *Malat1*, a long non-coding RNA, increased during

development, with the highest expression levesl being observed in adult microglia (**Extended Data Figs. 2a, b**). In the embryonic clusters, lysosome-related genes *Ctsb* (encoding cathepsin B), *Cstd* (encoding cathepsin D), *Lamp1* (lysosomal-associated membrane protein 1), were strongly induced in C1 and C2 microglia (**Fig. 3b and Extended Data Fig. 2c**), suggesting enhanced lysosomal activity in these embryonic microglia. In contrast, expression of *Apoe*, which encodes the myeloid cell activation marker apolipoprotein E (*27*), was enriched in the C1, C4 and C5 clusters (**Fig. 4b**). C6 microglia were characterized by high expression levels of *Tmsb4x* (encoding thymosin beta 4), *Eef1a1*, and *Rpl4* (**Fig. 4b and Extended Data Fig. 2d**), We next confirmed the existence of $APOE^{+}Iba1^{+}$ microglia and $CTSB^{+}Iba1^{+}$ microglia in the embryonic forebrain and cerebellum on a protein level by triple immunofluorescence staining (**Fig. 4c**). These distinct embryonic microglia subpopulations disappeared in the juvenile and adult brains (**Figs. 4c, d**). On the other hand, postnatal C9 and C10 microglia clusters were characterized by high expression of *Cst3* (encoding cystatin C, a cysteine protein proteinase inhibition family involved in neurodegenerative diseases of the CNS (*36*)), and *Sparc* (encoding secreted protein acidic and rich in cysteine; also known as osteonectin) (**Fig. 4e**). Immunolabeling for CST3 and SPARC confirmed the presence of $CST3^{+}SPARC^{+}Iba1^{+}$ microglia in the postnatal brains, whereas this population was virtually absent in embryonic forebrains (**Figs. 4f,g**). Interestingly, expression of CST3 was also detectable in a subpopulation of $Aldh1l1^{+}$ astrocytes in the adult cerebral cortex (**Extended Data Fig. 3**). In contrast to the juvenile cerebral cortex, where almost all microglia expressed CST3 and SPARC (**Figs. 4f, g**), the abundance of this microglia subpopulation slightly diminished in the adult cortex, as $CST3^{-}SPARC^{+}Iba1^{+}$ microglia emerged (**Fig. 4g**). In contrast, the proportion of $CST3^{+}SPARC^{+}Iba1^{+}$ microglia did not change between the juvenile and adult cerebellum (**Fig. 4g**), although the overall percentage of SPARC-expressing microglia was lower in the cerebellum than in cortex, and $CST3^{+}SPARC^{-}Iba1^{+}$ microglia made up a significant fraction of juvenile and adult cerebellar microglia (**Fig. 4g**). Taken together, our data identify novel markers of microglia subsets and demonstrate the

spatiotemporal and phenotypic diversity of microglia subsets during CNS development and homeostasis in the adult brain.

Identification of microglia clusters unique to demyelination and different from neurodegeneration

To investigate the kinetics of homeostatic microglia clusters and the putative generation of disease-specific microglia populations during CNS pathology, we compared a model of toxic demyelination, the cuprizone model, with a paradigm of neurodegeneration, the unilateral facial nerve axotomy (FNX) lesion (**Fig. 2a**). The blood–brain barrier remains intact in both models, and a loss of oligodendrocytes in the corpus callosum or a remote neurodegeneration within the facial nucleus, respectively, lead to local microglial activation without recruitment of circulating monocytes (*13, 37*). The two models allow us to study microglial plasticity following withdrawal of cuprizone or axonal regeneration, respectively (**Fig. 2a**).

On the *t*-SNE plot, microglia distributed uniformly in a major population, but cells that clustered separately were found 3 days after FNX, and in the 5- and 10-week groups of cuprizone treatment (**Fig. 5a-c**). The C11-13 microglia predominantly constituted the disease-associated separate clouds on the *t*-SNE map (**Fig. 5c**). Notably, the C11 microglia cluster was specific to neurodegeneration, whereas demyelination induced the disease-specific clusters (C12 and C13) (**Figs. 5d-f**). In the FNX model, the 3-day time point revealed a distinct microglia cluster (C11) characterized by stron expression of *Ctsc* (encoding cathepsin C) (**Fig. 5e**), whereas microglia from the 14-day time point clustered with the homeostatic microglia population. In contrast, toxic demyelination induced long-lasting transcriptional changes that only slightly recovered at the 10-week time point (**Fig. 5f**). In sum, our data suggest that homeostatic microglia are able to quickly change their phenotype and gain a discrete context- and time-dependent signature.

When analyzing the data for disease-specific signatures in microglia, a strong upregulation of *Apoe* was noted at all time points after cuprizone treatment (**Fig. 5g**). *Cst7* was more

prevalent in the demyelination-associated microglia (C12) (**Fig. 5g**), and *Cybb* was more strongly induced in the remyelination-associated C13 cluster (**Fig. 5h and Extended Data Fig. 4g**). In addition to *Apoe*, genes for *Axl*, *Igf*, *Lyz2*, *Itgax* (encoding CD11c), *Gpnmb* and *Apoc1* were induced during de- and remyelination (**Extended Data Fig. 4a**), whereas *Fam20c, Cst7, Ccl6, Fn1*, *Ank, Psat1* and *Spp1* were enriched to variable degrees in the demyelination-associated C12 microglia (**Figs. 5g,h and Extended Data Figs. 4b, c, e**). In contrast, the remyelination-associated C13 microglia was characterized by high expression levels of the MHC class II genes *Cd74, H2-A2* and *H2-Ab1* (**Fig. 5h and Extended Data Fig. 4i**). On the other hand, the microglial core marker *Tmem119* was down-regulated following cuprizone treatment (**Fig. 5h**). Single-molecular fluorescence in situ hybridization (smFISH) validated the disease-associated expression of *Fn1*, *Spp1*, *Cybb* transcripts in *Cx3cr1*-expressing microglia (**Extended Data Figs. 4d, f, h**). Furthermore, demyelination-associated microglia subtype ($SPP1^{+}CD74^{-}Iba1^{+}$ and $TMEM119^{-}CD74^{-}Iba1^{+}$) was confirmed on the protein level by triple immunofluorescence staining (**Figs. 5i,j**). Likewise, remyelination-associated microglia subtype ($SPP1^{-}CD74^{-}Iba1^{+}$ and $TMEM119^{-}CD74^{+}Iba1^{+}$) was confirmed by triple immunofluorescence staining (**Figs. 5i,j**). Overall, our results suggest the emergence of unique microglia subpopulations characterized by distinct signatures under defined disease conditions.

Microglial diversity in the human brain

In order to extend our studies of microglial heterogeneity from mice to humans, we next analyzed 1,180 cortical microglia isolated from surgically resected human brain tissue without histological evidence of CNS pathology (referred to as “healthy”) from five adult individuals with aged 23 to 54 years (**Suppl. Table. 1**). Unbiased hierarchical clustering of individual human microglia revealed four major clusters, hereafter referred to as healthy human clusters (HHu-C) (**Figs. 6a-c and Extended Data Fig. 5**). Detailed analysis of differentially regulated genes across the human microglia clusters revealed similarities with the gene expression profiles of murine homeostatic microglia. For example, *CST3* (enriched

in mouse clusters C9 and C10) was more highly expressed in HHu-C1 and HHu-C2 than in HHu-C3 and HHu-C4 (**Figs. 6b, d**). In contrast, the human microglia cluster HHu-C4 showed comparatively high expression of the chemokine genes *CCL4* and *CCL2*, and the zinc finger transcription factors *EGR2* and *EGR3* (**Figs. 6b, d**). Interestingly, *CCL4* mRNA was rarely expressed in murine microglia even after cuprizone treatment (**Extended Data Fig. 4j**). Notably, *P2RY13* mRNA was highly expressed by human microglia HHu-C1 and HHu-C2 clusters (**Fig. 6b, Extended Data Fig. 5c**), whereas the gene was not differentially expressed by murine adult microglia at single-cell level. In sum, our analysis identified homeostatic human microglia states with distinct gene expression patterns that partially overlap with adult mouse microglia.

Activated microglia have been implicated in disease progression of multiple sclerosis (MS), a debilitating neurological disorder associated with demyelination (*38*). To examine the presence of disease-specific microglia subpopulations during this pathology in humans, 422 $CD45^+$ cells isolated from the brains of five patients with histologically confirmed early active MS (**Extended Data Fig. 6**) were subjected to scRNA-seq and subsequently analysed together with healthy human microglia (**Figs. 6e-j**). Unsupervised clustering grouped cells into ten transcriptionally different clusters, which we termed human clusters (Hu-C)1-10 (**Figs. 6f-h**). Among them, the transcriptome of the Hu-C1 population showed a strong lymphocyte signature (*TRAC, TRBC2, CD52, and IL32*) (**Fig. 6i**), and the Hu-C9 and Hu-C10 populations were characterized by a clear monocytic profile (*PLAC8, S100A9, CLEC12A*, and *CCR2*) (**Fig. 6i**); these clusters were therefore excluded from further analysis. The remaining seven myeloid clusters, Hu-C2-8, expressed microglial core genes such as *TMEM119*, *P2RY12*, *CX3CR1*, *SLC2A5* and *P2RY13* to variable degrees (**Fig. 6g**). The Hu-C5-7 microglia clusters, which consisted entirely of microglia from healthy brains, showed highest expression levels of the microglial core genes and were therefore considered to represent the homeostatic microglia states (**Figs. 6h, j and Extended Data Fig. 7a**). Interestingly, the Hu-C4 subset that was shared by microglia from the healthy and diseased human brains revealed reduced expression levels of the core signature genes, but elevated

levels of *CCL2*, *CCL4*, *EGR2* and other chemokine/cytokine genes, suggesting a pre-activated state of these microglial cells (**Figs. 6h, j and Extended Data Fig. 7d**). Unbiased clustering further identified two MS-enriched microglia clusters (Hu-C3 and Hu-C8) and one MS-associated microglia cluster (Hu-C2) that were clearly separated from the homeostatic clouds on *t*-SNE plots (**Figs. 6e, f, h, j**). The microglia clusters Hu-C2, Hu-C3 and Hu-C8 showed increased expression of *APOE* and *MAFB* (**Extended Data Fig. 7f**), whereas the core microglial genes were down-regulated or absent (**Fig. 6j**). Immunofluorescence staining of tissue from MS patients confirmed the strong reduction of TMEM119 expression on microglia in demyelinating lesions (**Fig. 6k**). The MS-associated Hu-C2 microglia was characterized by high expression levels of *CTSD, APOC1*, *GPNMB*, *ANXA2, FAM20C* and *LGALS1* genes (**Fig. 6j and Extended Data Fig. 7b, f**). The Hu-C3 microglia showed increased gene expression of MHC class II-related molecules, such as *CD74*, *HLA-DRA*, *HLA-DRB1* and *HLA-DPB1* (**Fig. 6j and Extended Data Fig. 7c**). This suggests an immunoregulatory role, reminiscent of the remyelination-associated microglia subtype (C13) in mice (**Fig. 5**). Finally, the Hu-C8 microglia showed strong expression of *SPP1*, *PADI2* and *LPL* genes, similar to the demyelination-associated microglia subtype (C12) in mice (**Figs. 6g, j and Extended Data Fig. 7e**). Of note, pairwise correlation analysis of mouse and human microglia orthologs confirmed that human MS-associated/-enriched microglia clusters (Hu-C2, Hu-C3 and Hu-C8), but not the pre-activated Hu-C4 cluster, are transcriptionally correlated to mouse demyelination-associated (C12) and remyelination-associated (C13) microglia observed after cuprizone treatment (**Extended Data Fig. 8**)

To validate our scRNA-seq results for human microglia from MS patients, we performed immunohistochemical staining of MS brain sections. First, we stained for MRP14, which is known to label infiltrating monocytes but not microglia in early active lesions (*39*). Human brain sections without CNS pathology were virtually devoid of $MRP14^{+}Iba1^{+}$ cells, whereas 12 % of all $Iba1^{+}$ cells in the MS sections were infiltrating monocytes (healthy: 0.2 ± 0.2 %, MS: 11.6 ± 2.4 %, **Fig. 6l**). However, this indicates that the vast majority of $Iba1^{+}$ myeloid cells present in these sections were resident human $MRP14^{-}Iba1^{+}$ microglia. Next, we

performed triple immunofluorescence staining and identified $CTSD^{+}MRP14^{-}Iba1^{+}$, $SPP1^{+}MRP14^{-}Iba1^{+}$ and $CD74^{+}MRP14^{-}Iba1^{+}$ microglia subsets as part of the Hu-C2, Hu-C8 and Hu-C3 clusters in brain sections from MS patients (**Figs. 6m, n**). In contrast to the mouse cuprizone-induced demyelination model, the proportion of SPP1-, CTSD- and CD74-expressing microglia subsets varied substantially between individual MS patients (**Figs. 6m, n**), indicating high inter-individual heterogeneity. Together, these findings suggest the existence of distinct disease-related microglia subtypes in the brains of MS patients, which are phenotypically similar to murine microglia subtypes in a demyelination model.

DISCUSSION

Our study provides a high-resolution view of the transcriptional landscape of microglia subtypes across multiple regions of the adult murine CNS. Furthermore, our data reveal a transcriptional continuum between microglia states, with few pre-existing clusters under homeostatic conditions after birth. Initial cell-specific states were rather uniform throughout the CNS during adulthood. In contrast, microglia subtype specification after birth emerged in a region- and disease stage-specific manner with high plasticity (**Extended Data Fig. 9**). Each brain region appears to be subject to changes in its immunological status, as revealed by regionally distinct states of mature microglia. In fact, classical monogenetic microgliopathies, such as hereditary diffuse leukoencephalopathy with spheroids (HDLS), Nasu-Hakola disease and others, are characterized by variable regional pathologies, suggesting diversity and differential spatial vulnerability of microglia (*4, 36*). Our data also reveal considerable dynamics of microglia subsets during development. It has been suggested that microglia ontogeny follows a defined stepwise transcriptional program to achieve the full homeostatic signature after birth (*7, 25, 40*). Indeed, we observed that microglia core genes like *Tmem119, Selplg* and *Slc2a5* are abundantly expressed only during adulthood. Since their expression levels increase after birth, it is tempting to speculate that microglia from juveline might not yet have fully matured. Interestingly, the embryonic microglia clusters were characterized by high expression of *ApoE* (C1, C4 and C5) and *Ctsb* (encoding cathepsin B) (C1 and C2), suggesting increased microglial activation and phagocytic–lysosomal activity. The developmental upregulation of cathepsin B, a protease activates matrix metalloproteinases (MMPs) and is thereby essential for the proteolysis of extracellular matrix components, might facilitate microglial movement in the growing brain, which depends on MMP8 and MMP9 *in vivo* (*7*). The widespread presence of cathepsin B^+ microglia across different regions of the developing forebrain and cerebellum suggests a general function of these proteins in embryonic microglia. Furthermore, differential enrichment of microglial clusters across CNS regions during development might reflect distinct maturation stages of these regions.

Previous studies on regional variations in microglial density (*41*), surface expression of a small panel of immune molecules (*20*), dependency on interleukin-34 (*42*), and microarray analysis of microglial bulk RNA (*21*) suggested diversity of microglia. However, earlier studies based on analysis of bulk cell populations isolated using a small set of surface markers were limited in their resolution of the heterogeneity and complexity of CNS immune cells. scRNA-seq enables unbiased characterization of small cell populations, and was used here to generate a high-resolution picture of microglia heterogeneity in the mouse and human brain. Single-cell analysis can also help to identify novel markers, pathways and regulatory factors that are critical during CNS development, homeostasis and disease. For example, in a recent study combining fate mapping and scRNA-seq, we showed that CAMs, like pvMΦ, are ontogenetically closely related to microglia (*8*). Despite their ontogenetic resemblance, this study revealed that microglia and pvMΦ are transcriptionally distinct myeloid cell populations in the CNS. Whether microglia and CAMs also originate from distinct progenitor populations in the yolk sac needs to be elucidated in the future.

A recent study proposed regional differences in deep brain murine microglia, such as those within the basal ganglia (*43*). Microglia from the nucleus accumbens, ventral tegmental area and other regions were found to differ in morphology, density and membrane properties. Whether the observed differences in the membrane properties of microglia subsets within basal ganglia are functionally relevant remains unclear. Notably, morphological differences of microglia were accompanied by variations of cell density, with highest numbers of microglia in the midbrain and basal ganglia, as has been described previously (*41*). These region-specific features might be due to the specific local microenviroment. In our study, we used scRNA-seq to investigate different CNS regions (excluding the basal ganglia) in the adult mouse brain that are known to exhibit microglia with diverse morphological features; however we did not observe obvious changes at the transcriptional level. The only exception was an enrichment of the C7 and C8 clusters in the cerebellum. Notably, the expression of *Sparc*, one of the representative genes that can segregate postnatal microglia states, was lower in cerebellar microglia compared to their cortical counterparts. These findings are in line with

Affymetrix analyses that suggested heterogeneity of murine cerebellar microglia (*21*). Moreover, recent single-nuclei sequencing of striatal and cerebellar microglia from adult mice revealed epigenetic regulation of microglia clearance activity, with highest clearance activities in cerebellar microglia (Ayata 2018).

Previous single-cell analyses identified neurodegeneration-associated microglia subsets in mice (*27, 32, 33*), but deyelination- and remyelination-associated microglia subsets were never examined at the single-cell level before. Here, we provide evidence for highly specialized and distinct demyelination- and remyelination-associated microglia subtypes in mice. Notably, we detected transcriptionally similar microglia subclasses in brain tissue from human MS patients, suggesting conserved responses to CNS demyelination. Since microglia down-regulate the expression of core genes during inflammatory conditions, we took advantage of the recently established microglia markers, TMEM119 and P2Y12R, that allow for the distinction of human microglia from infiltrating monocytes (*44, 45*). Our findings suggest that the highly specialized MS-associated human microglia subpopulations are characterized by enriched expression of *SPP1*, *CTSD* and the MHC class II-related molecule *CD74*, providing potential novel targets for MS therapy.

Taken together, our study provides the first *in vivo* comparison of microglia heterogeneity at a single-cell resolution in the mouse and human CNS. Although we detected transcriptionally distinguishable microglia subpopulations, these did not appear as distinct clusters but rather as a transcriptional continuum of the local microglia population. This might represent the transcriptional basis for the ability of microglia to swiftly adapt to environmental changes. Our data further indicate that microglial responses to pathology are not uniform, but are shaped by the underlying pathology. In fact, we found disease-associated microglia subtypes in mice and humans that differed between neurodegenerative conditions (such as FNX) and toxic demyelination (like cuprizone). The appearance of context-dependent microglia subtypes with their own specific transcriptional profiles has potential therapeutic implications. Moreover, by establishing the transcriptional profile of heterogenous microglia populations in

434 healthy and diseased rodents and humans, our study may provide new insights into the
435 pathogenesis of CNS diseases.
436

ACKNOWLEDGEMENTS

We thank Maria Oberle, Margarethe Ditter, Tina el Gaz and Jan Bodinek-Wersing for excellent technical assistance, and Christina Gross for proofreading. Special thanks to Amit Zeisel and Sten Linnarsson, Division of Molecular Neurobiology, Department of Medical Biochemistry and Biophysics, Karolinska Institutet, Stockholm, Sweden for sharing data and support. T.M. was supported by the KANAE Foundation for the Promotion of Medical Science, and the Japan Society for the Promotion of Science (JSPS) as the JSPS Postdoctoral Fellow for Research Abroad. M.P. is supported by the Sobek Foundation, the Ernst-Jung Foundation, the DFG (SFB 992, SFB1160, SFB/TRR167, Reinhart-Koselleck-Grant), the Ministry of Science, Research and Arts, Baden-Wuerttemberg (Sonderlinie "Neuroinflammation") and the BMBF-funded competence network of multiple sclerosis (KKNMS). J.P. is supported by the DFG (SFB/TRR167 B05 and B07), BIH CRG 2a, and the UK DRI Momentum Award. C.S. is supported by the DFG (STA1389/2-1), the Deutsche Multiple Sklerose Gesellschaft (DMSG), the National MS Society of the USA (NMSS) and the Hertie-Foundation. C.B. is supported by the DFG (SFB/TRR167 B05).

AUTHOR CONTRIBUTIONS

TM, RS, OS, CB, LA, CS, SN, PK, GvL, VAC, PCR, AM, US and RG conducted experiments and analyzed the data. MP, CS and JP analyzed the data, contributed to the in vivo studies and provided mice or reagents. TM and MP supervised the project and wrote the manuscript.

MATERIAL AND METHODS

Mice: CD1 mice were used. All animal experiments were approved by local administration and were performed in accordance to the respective national, federal and institutional regulations. Detailed mouse information is provided in Suppl. Table 1.

Analysis of single cell gene expression in diverse CNS cell types: A CNS cell suspension was obtained from a thorough preparation of eight different regions of the juvenile brain (mixed gender) in which meninges and choroid plexus were removed before. Cells were then subjected to single-cell RNA-seq using the C1 AutoPrep instrument (Fluidigm) and STRT/C1 protocol, as previously described (Zeisel et al., 2015; Goldmann et al., 2016). Each single cell was imaged and manually curated, and only single healthy-looking cells without debris were used for the analyses. Data analysis was performed as previously described (doi: DOI: 10.1126/science.aaa1934) using the BackSPIN algorithm.

Single-cell RNA-seq for mouse microglia: Microglia were FACS-sorted from up to six different CNS regions of healthy and diseased brains (see gating strategy shown in supplementary Fig. 1) into a 384-well plate containing a lysis buffer, and were analysed using Smart-seq2 method. Expression profiles were obtained as absolute cDNA molecule counts using the STAR aligner (doi: 10.1093/bioinformatics/bts635) to align raw sequences in conjunction with feature counts as part of the subread package (doi: 10.1093/nar/gkt214) to obtain gene counts. Further analysis and data normalization was performed using the RaceID package (Herman JS 2018). Clusters with more than ten individual cells were retained for further analysis and normalized to “transcripts per million” to compensate for differences in total transcriptome size between cell types. Heatmaps were generated using the online software (https://academic.oup.com/bioinformatics/article/32/18/2847/1743594).

Analysis of microglia from human brains: Human microglia were isolated from histologically healthy brain tissue removed during brain surgery for the treatment of epilepsy in five individuals (these tissues are not part of the epileptic region but are routinely removed to surgically access the epileptic lesion). Histopathological changes were excluded by an experienced neuropathologist, and only histologically healthy specimens were included in this study. Microglia were FACS-sorted into a 384-well plate containing lysis buffer. Single-cell RNA sequencing was conducted using the Cel-Seq2 protocol and processed as previously described (*46*). Libraries were sequenced on an Illumina HiSeq 3000 System in high output run mode at a depth of ~200,000 reads per cell. Paired end reads were aligned to the transcriptome using bwa with default parameters and all isoforms of the gene counted to a single gene locus (*47*). Reads that were not uniquely mapped were discarded. The left read contained the barcode information (6 bases corresponded to the cell specific barcode + 6 bases representing the unique molecular identifier (UMI)) and a polyT stretch and was

omitted from quantification. The corresponding right read was mapped to the ensemble of all gene loci and used for quantification. Genes were counted based on the number of UMIs per transcript from a given gene locus. The number of UMIs was converted to transcript counts based on a binomial distribution (*48*). The aggregate of transcript counts with the same cell barcode represented the transcriptome of an individual cell. Data analysis, normalization and visualization was performed using the RaceID2 package (doi:10.1038/nature14966). Clusters with more than 15 individual cells were retained for further analysis and transcript counts were normalized by down sampling to 1500. Detailed human patient information is provided in Suppl. Table.1.

Flow cytometry: After transcardial perfusion with PBS, brains were roughly minced and homogenized with a potter in HBSS containing 15 mM HEPES buffer and 0.54 % glucose. Whole-brain homogenate was separated by 70/37/30 % layered Percoll gradient centrifugation at 800 *g* for 30 min at 4 °C (no brake). The CNS macrophages containing interphase was then collected and washed once with PBS containing 2 % FCS and 10mM EDTA before staining. Cells were stained with primary antibodies directed against CD11b (M1/70, BioLegend), CD45 (30-F11, BD Biosciences), Ly6C (AL-21, BD Biosciences) and Ly6G (1A8, BD Biosciences) for 20 min, and CD206 (C068C2, BioLegend) for 45 min at 4 °C. After washing, cells were sorted using a MoFlo Astrios (Beckman Coulter). Viable cells were gated by staining with Fixable Viability Dye (eBioscience). Data were acquired with FACSDiva software (Becton Dickinson). Post-acquisition analysis was performed using FlowJo software, version X.0.7.

Immunohistochemistry and cell quantifications: For juvenile and adult mice, after transcardial perfusion with PBS, brains were fixed for 4 h in 4 % PFA, dehydrated in 30 % sucrose and embedded in Tissue-Tek® O.C.T. compound (Sakura Finetek Germany GmbH). For embryos, isolated brains were fixed for 4 h in 4 % PFA, dehydrated in 30 % sucrose and embedded in Tissue-Tek® O.C.T. compound. Cryosections were obtained as described previously (*26*). Sections were then blocked with PBS containing 5 % bovine serum albumin and permeabilized with 0.1% Triton-X 100 in blocking solution. Primary antibodies were added over night at a dilution of 1:500 for Iba-1 (ab178846, Abcam), 1:200 for APOE (AB947, Millipore), 1:200 for CTSB (ab58802, Abcam) 1:200 for CST3 (AF1238, R&D Systems), 1:200 for SPARC (IC942G, R&D Systems), 1:400 for NeuN (MAB377, Millipore), 1:1000 for APC (OB80, Millipore), 1:100 for Aldh1l1 (ab87117, Abcam), 1:500 for TMEM119 (ab209064, abcam), 1:500 for SPP1 (ab8448, abcam), 1:200 for CD74 (In1/CD74, BioLedend) at 4°C. Secondary antibodies were purchased from Thermo Fisher Scientific added as follows: Alexa Flour® 488 1:500, Alexa Flour® 568 1:500 and Alexa Fluor® 647 1:500 for 2h at RT. Human tissue blocks were fixed in 4 % PFA overnight and embedded in paraffin. Sections were then blocked with PBS containing 5 % bovine serum albumin and

permeabilized with 0.1% Triton-X 100 in blocking solution. Primary antibodies were treated over night at a dilution of 1:500 for Iba-1 (ab178846, Abcam; ab139590, Abcam; NB100-1028, Novus Biologicals), 1:200 for SPP1 (HPA027541, Sigma), 1:500 for CD74 (ab9514, abcam), 1:500 for CTSD (ab6313, abcam), 1:200 for MRP14 (T-1026, BMA Biomedicals; LS-B12844, LSBio). Secondary antibodies were purchased from Thermo Fisher Scientific added as follows: Alexa Flour® 405 1:500, Alexa Flour® 488 1:500, Alexa Flour® 568 1:500 and Alexa Fluor® 647 1:500 for 2 h at RT. Coverslips were mounted with/without ProLong™ Diamond Antifade Mountant with DAPI (Thermo Fisher Scientific). Images were taken using a conventional fluorescence microscope (Olympus BX-61 with a color camera (Olympus DP71) or BZ-9000 (Keyence, Osaka, Japan) and the confocal pictures were taken with Fluoview FV 1000 (Olympus) using a 20 x 0.95 NA (XLUMPlanFL N, Olympus).

Facial nerve axotomy and cuprizone model of demyelination and remyelination: Facial nerve was injured as described previously (*13, 37*). Briefly, mice were anesthetized by subcutaneous injection of a mixture of ketamine (50 mg/kg) and xylazine (7.5 mg/kg), and the right facial nerve was transected at the stylomastoid foramen, resulting in ipsilateral whisker paresis. Cuprizone treatment was used as a model of toxic, demyelination and remyelination (*37, 49*). For demyelination, mice were fed for 5 weeks with 0.45 % (wt/wt) cuprizone (Sigma, St. Louis, MO) in the ground breeder chow. For remyelination, the cuprizone diet was discontinued after 5 weeks and animals were maintained for further 5 weeks under normal diet to allow spontaneous remyelination. Untreated age-matched mice were used as control.

Single molecule fluorescent in situ hybridization (smFISH): Mice were perfused with PBS, followed by 4% paraformaldehyde (PFA). The brain tissues were harvested and immersion-fixed in 4% PFA for 3 h, and subsequently were put into 30% sucrose in 4% PFA at 4°C overnight, and embedded in OCT for sectioning, frozen on dry ice and stored at -80°C until used. 10-µm thick sections mounted on the glass plate were washed 3 times with PBS, and treated with pre-chilled methanol for 10 min at -20 °C. Then the slides were incubated for 10 min at 70°C in Tris-EDTA (pH 8.0), and the sections were washed with SSC 2X and incubated for 4 hr with hybridization buffer containing 250 nM fluorescent label probes (LGC Biosearch Technologies) at 38.5°C. After 4 times washing with 20% formamide wash buffer containing SSC 2X, the slides were mounted with Prolong Gold containing DAPI. Stack Images were taken using a Olympus BX-61 microscope.

Gene ontology (GO) enrichment analysis: The defined differentially regulated genes were analyzed using the software (available from http://metascape.org/gp/#/main/step1).

Pairwise correlation analysis: Comparison between human and mouse data was performed by selecting all genes found to differentially expressed by RaceID (adjusted

570 p<0.01, log2FC > 1) in any of the identified clusters. For genes from the human dataset
571 mouse orthologs were identified from the NCBI HomoloGene database
572 (https://www.ncbi.nlm.nih.gov/homologene), using the annotationTools R package (Kuhn A
573 2008); the same was done to identify human orthologs for the murine genes. All human
574 genes with a ortholog in the mouse set as well as all murine genes with an ortholog in the
575 human set were kept. Canonical Cluster Analysis as implemented in the Seurat package
576 (Butler A 2018) was then performed on the 768 common genes identified in this manner.

577 **Statistical analysis:** Statistical significance was determined using one-way ANOVA with
578 *post hoc* Tukey Multiple Comparison test using GraphPad Prism 5.04 software.

579

FIGURE LEGENDS

Figure 1: Unbiased single-cell RNA-seq of CNS cells reveals specific profiles of murine microglia and pvMΦ.

(a) Schematic diagram showing the isolation of single CNS cells from juvenile (3 weeks of age) mice for unbiased sampling and single-cell RNA-seq (scRNA-seq).

(b) Cluster analysis using *t*-SNE of 3,047 individual cells measured by single-cell RNA sequencing and bi-clustering. Each dot represents an individual cell. The populations of microglia and perivascular macrophages (pvMΦ) are marked by a dotted line. Vsmc: vascular smooth muscle cell.

(c) Heat map showing clustering of 2,996 single cells, featuring 49 most variable genes. Selected marker genes enriched in each cell-type representing expression levels of selected known and novel markers are shown on the right.

(d) *t*-SNE clustering plots of individual microglia and perivascular macrophages (pvMΦ) showing distinct gene expression pattern between the two cell types in the juvenile CNS (326 cells). Each dot represents a single cell. Microglia are depicted as circles, pvMΦ as triangles.

Figure 2: Comprehensive analysis of microglial diversity by single-cell RNA-sequencing.

(a) Illustration depicting the workflow for the isolation of microglia from different CNS regions of embryonic (embryonic day E16.5) and juvenile (3 weeks of age) and adult (16 weeks) mice during homeostasis and during pathology, namely facial nerve axotomy (FNX) cuprizone-mediated demyelination for scRNA-seq.

(b) *t*-SNE plot showing all analyzed microglia cells from different conditions tested in this study. Each dot represents a single cell.

(c) *t*-SNE plot depicting 13 clusters for all different conditions. Colors represent each cluster (C).

Figure 3: Identification of spatiotemporal subclasses of microglia in the mouse.

(a) *t*-SNE plot of 2,966 individual microglia isolated at different time points of development. Each dot represents a single cell. Colors correspond to the time points investigated.

(b) *t*-SNE plot depicting ten major and three minor microglia clusters at three different developmental stages. Each dot represents a single cell. Colors represent each cluster (C).

(c) Heat map of top differentially regulated genes that were up- or down-regulated in each cluster, including genes such as *Malat1*, *Selplg*, *Tmem119*, *Sparc*, *Cst3*, *Ctsd*, *Lamp1*, *Ctsb*, *Apoe*, *Tmsb4x*, *Eef1a1* and *Rpl4*.

(d) *t*-SNE plots depicting regional distribution of transcripts from 2966 individual microglia at different developmental time points. Each dot represents a single cell.

(e) Distribution of microglia clusters among different CNS regions during embryonic and postnatal stages. Colors represent distinct clusters.

Figure 4: Characteristics of microglial subsets during development.

(a) *t*-SNE plots depicting the expression kinetics of the microglial core genes *Tmem119*, *Selplg* and *Slc2a5* during ontogeny. Upper right cloud shows E16.5 microglia whereas the lower left cloud represents microglia from juvenile and adult mice. Color key indicates the expression levels.

(b) *t*-SNE plots of embryo-enriched microglia transcripts for *Ctsb, Apoe* and *Tmsb4x*.

(c) Representative immunofluorescence images for apolipoprotein (Apo)E, cathepsin B (CTSB) and ionized calcium-binding adapter (Iba)1 in the embryonic forebrain and juvenile cortex. Dotted frame 1 indicates $ApoE^{-}CTSB^{-}Iba1^{+}$ embryonic microglia (representing clusters C3, C6). Frame 2 illustrates $ApoE^{-}CTSB^{+}Iba1^{+}$ embryonic microglia (C1, C2) whereas frame 3 shows $ApoE^{+}CTSB^{+}Iba1^{+}$ triple-positive embryonic microglia (C1). Dotted frame 4 depicts $ApoE^{+}CTSB^{-}Iba1^{+}$ embryonic microglia (C4, C5). Frame 5 illustrates $ApoE^{-}CTSB^{-}Iba1^{+}$ microglia (white arrowheads) found at the juvenile stage. Yellow arrowheads indicate $ApoE^{+}Iba1^{-}$ cells in the juvenile brain. Representative pictures out of four investigated mice are shown. Scale bars: 50 µm (overview), 30 µm (insert).

(d) Quantification of ApoE and CTSB immunoreactivities in $Iba1^{+}$ microglia from different CNS regions during development. Bars represent means ± SEM from four animals (541-853 microglia per region).

(e) *t*-SNE plots-based distribution of *Cst3* and *Sparc* transcripts in microglia. Color keys indicate the expression levels.

(f) Representative immunofluorescence images for cystatin C (CST3), secreted protein acidic and rich in cysteine (SPARC) and Iba1 in the embryonic forebrain, juvenile and adult cortex. Frame 1 indicates $CST3^{+}SPARC^{+}Iba1^{+}$ microglia (representing clusters C9, C10) whereas frame 2 highlights $CST3^{-}SPARC^{-}Iba1^{+}$ microglia (C7) during adulthood. Representative pictures out of four investigated mice are shown. Scale bars: 50 µm (overview), 20 µm (insert).

(g) Quantification of CST3 and SPARC immunopositivity in microglia from different regions of the CNS at distinct developmental time points. Bars represent means ± SEM from four animals (569 - 1961 microglia per region).

Figure 5: Specific disease-associated microglia populations with distinct kinetics during demyelination and neurodegeneration.

(a) Projection of 1,564 single microglia isolated from different CNS regions during homeostasis or FNX or cuprizone treatment as *t*-SNE plot.

(b) Heat map of top differentially regulated genes that were up- or down-regulated in each cluster. Highest differentially expressed genes are highlighted.

(c) *t*-SNE plot exhibiting 13 clusters for the 1,564 individual microglia isolated from different CNS regions during homeostasis or FNX or cuprizone treatment.

(d) Left: Kinetics of facial nucleus (FN) microglia subpopulation on a *t*-SNE map either untreated (FN-normal) or after 3 days post FNX (FNX-d3) or 7 days post FNX (FNX-d14), respectively. Right: Histogram displaying proportion of microglia clusters either untreated (FN-normal) or after FNX-d3 or FNX-d14.

(e) Clustering of the *Ctsc* gene expression following FNX. Expression of *Ctsc* is found to be upregulated in C11 at FNX-d3. The color key indicates the expression levels. Insert: close-up of the C11.

(f) Persistent transition of corpus callosum (CC) microglia population on a t-SNE map before (CC-normal) and after demyelination (CC-Demyelination) or remyelination (CC-Remyelination). Close-ups reveal distribution of clusters after demyelination and remyelination. Right: Histogram showing long-lasting changes in microglia populations following cuprizone treatment.

(g) Kinetics of *Apoe, Cst7* and *Cybb* expression after cuprizone challenge displayed in *t*-SNE plots. Color keys represent the respective expression levels.

(h) *t*-SNE plots for *Tmem119, Spp1, Cd74* after cuprizone treatment. *Tmem119* is downregulated following treatment, whereas *Spp1* is upregulated in C12, and *Cd74* mRNA is increased in C13. Color keys indicate the expression levels.

(i) Left: representative immunofluorescence images for osteopontin (secreted phosphoprotein 1, SPP1), CD74 and Iba1 in the normal and demyelinated corpus callosum. Arrowheads indicate $SPP1^{-}CD74^{-}Iba1^{+}$ (white arrowheads), $SPP1^{+}CD74^{-}Iba1^{+}$ (red arrowheads), and $SPP1^{-}CD74^{+}Iba1^{+}$ (blue) parenchymal microglia, respectively. Representative pictures out of three or four investigated mice are shown. Right: Quantification thereof. Bars represent means ± SEM of three to four animals (437 - 825 microglia per condition). Each symbol represents one animal. Scale bars: 30 µm.

(j) Left: typical immunofluorescence pictures for transmembrane protein (TMEM) 119, CD74 and Iba1 in the normal and demyelinated corpus callosum. Arrowheads show $TMEM119^{+}CD74^{-}Iba1^{+}$ (white arrowhead), $TMEM119^{-}CD74^{-}Iba1^{+}$ (red) and $TMEM119^{-}CD74^{+}Iba1^{+}$ (blue) parenchymal microglia. Representative pictures out of four investigated mice are shown. Right: Quantification thereof. Bars represent means ± SEM of four animals (808 - 1024 microglia per condition). Each symbol represents one animal. Scale bars: 30 µm.

Figure 6: Presence of distinct subclasses of microglia in healthy human and MS brains.

(a) *t*-SNE plot of 1,180 individual human microglia isolated from five individual non-pathological brains depicts four major clusters (HHu-C1-4). HHu-C: healthy human microglia cluster. Each dot represents a single cell. Colors correspond to each cluster.

(b) Heat map of the top differentially regulated genes that were up- or down-regulated in each cluster, including genes such *CST3, P2RY13, CCL4, CCL2, EGR2* and *EGR3*.

(c) Bar graphs representing the relative abundance of microglia cells in the respective clusters from five individual non-pathological brains. Colors represent distinct clusters.

(d) *t*-SNE plots for *CST3, CCL4* and *EGR2 mRNA* expression. *CCL4* and *EGR2* are enriched in the Hu-C4.

(e) *t*-SNE plot of 422 individual human microglia isolated from five individual non-pathological brains and five patients with early active multiple sclerosis (MS). Each dot represents a single cell. Colors correspond to each condition or patient.

(f) *t*-SNE plot depicting ten major clusters (Hu-C1-10) of microglia from healthy and diseased individuals. Each dot represents a single cell. Colors correspond to each cluster.

(g) Heat map of all differentially regulated genes that were up- or down-regulated in each cluster.

(h) Bar graphs representing the relative abundance of microglia in each cluster from healthy and individual MS patients. Colors represent individual patients or conditions.

(i) *t*-SNE plots representing the core signature genes for lymphocytes, myeloid cells and monocytes in the brains from MS patients. Color keys reflect the expression levels.

(j) *t*-SNE plots of the microglia cluster representing the top five enriched genes for each cluster. Homeostatic microglial genes are enriched in the microglia clusters Hu-C5-7, whereas Hu-C4 is characterized by the expression of proinflammatory molecules *CCL4* and *CCL2*. Hu-C2, Hu-C3 and Hu-C8 are present in microglia from MS patients.

(k) Immunofluorescence images for TMEM119 and Iba1 in healthy or MS patient brains. Arrowheads indicate $TMEM119^{+}Iba1^{+}$ cells (filled) in the healthy brains, and $TMEM119^{-}Iba1^{+}$ microglia (open) during MS. Scale bar: 50 µm.

(l) Representative immunofluorescence pictures for Iba1^{+}MRP14^{-} (indicating microglia) and Iba1^{+}MRP14^{+} cells (representing infiltrating early activated monocytes) in the normal and MS brain. Inserts show microglia (first row) and monocytes (second row) in the MS lesion. Right: Quantification thereof. Bars represent means ± SEM. Each symbol represents one patient. Scale bars: 50 µm (overview), 4 µm (insert).

(m) Upper panel: representative immunofluorescence images for SPP1, CTSD, Iba1 and MRP14 indicating microglia subsets in normal and MS brains. Representative pictures out of four individuals were chosen. Dotted frames represent SPP1^{-}CTSD^{+}MRP14^{-}Iba1^{+} microglia (1) and SPP1^{+}CTSD^{-}MRP14^{-}Iba1^{+} microglia (2). Scale bars: 50 µm (overviews), 20 µm (inserts). Lower panel: Quantification of microglia immunoreactivities in healthy or MS brains. Percentages indicate the relation of MRP14^{-}Iba-1^{+} microglia subsets in individual brains. 153 - 163 microglia per patient were examined.

(n) Upper: Immunofluorescence pictures for SPP1, CD74, Iba1 and MRP14 for the characterization of microglia cluster in healthy and MS brains. Colored dotted frames indicate SPP1^{-}CD74^{+}MRP14^{-}Iba1^{+} (white), SPP1^{+}CD74^{-}MRP14^{-}Iba1^{+} (yellow) parenchymal microglia, respectively. Representative pictures out of four individuals are shown. Scale bars: 50 µm (overviews), 20 µm (inserts). Lower left: Quantification of microglia immunopositivities in healthy or MS brains. Percentages indicate the relation of MRP14^{-}Iba-1^{+} microglia subsets in individual brains. 152 - 200 microglia per patient were investigated. Lower right: Distribution of SPP1 and CD74-reactive Iba1^{+} microglia subsets in the healthy mouse corpus callosum or during cuprizone-induced de-and remyelination as shown in Fig. 5i.

EXTENDED DATA

Extended Data Figure 1: Molecular characterization of rodent microglia and perivascular macrophages.

(a) Heat map showing clustering of 2,996 single cells, featuring ten selected genes enriched both in microglia and perivascular macrophages (pvMΦ) obtained from juvenile (3 weeks of age) mice.

(b) Gene ontology (GO)-term enrichment analysis for the 274 top genes enriched for microglia.

(c) GO-term enrichment analysis for the top 317 genes enriched for pvMΦ.

Extended Data Figure 2: Microglial subpopulations in mice with distinct gene expression during development.

(a) Distribution of *Malat1 g*ene expression in a *t*-SNE plot. Color keys represent the respective expression levels. Upper left cloud represents embryonic microglia population whereas lower right cloud combines both juvenile and adult microglia as shown in Fig. 2b.

(b) Left: smFISH for *Malat1* and *Cx3cr1* shows the kinetics of *Malat1*$^{+}$ microglia during development. Scale bar: 10 µm. Representative pictures out of two investigated adult mice are shown. Yellow arrowhead and white indicate *Malat1*$^{+}$*Cx3cr1*$^{+}$ microglia and *Malat1*$^{+}$*Cx3cr1*$^{-}$ non-microglia cells, respectively. Right: Frequency of *Malat1*$^{+}$ microglia in the forebrain or cortex during development. Bar represents mean ± SEM of 120 studied cells from three animals per time points.

(c) *t*-SNE plot of *Ctsd* and *Lamp1* gene expression that were enriched in C1 and C2 clusters as shown in Fig. 2c.

(d) *t*-SNE plot of *Eef1a1* and Rpl4 gene expression that were enriched in C6 cluster as shown in Fig. 2c.

Extended Data Figure 3: Cst3 is enriched in adult microglia.

(a-c) Representative sections of the cortex from adult mice using immunofluoresence for cystatin C (CST3, green), NeuN for neurons (red, a), adenomatous polyposis coli (APC) for oligodendrocytes (red, b), respectively. The astrocyte marker Aldh1l1 (red, c) combined with CST3 was used on the hippocampal sections. Scale bars: 50 µm (overviews) and 20 µm (magnifications). Representative pictures out of three investigated mice are shown.

(d) Quantification of CST3 immunoreactivity in the brain of adult mouse. Bar represents mean ± SEM of three animals (393 microglia, 1817 neurons, 298 oligodendrocytes, 461 astrocytes).

Extended Data Figure 4: Molecular characterization of microglia subpopulations during de- and remyelination.

t-SNE plots showing expression of *Axl, Igf1, Lyz2, Itgax, Gpnmb, Apoc1* (**a**), *Fam20c Ccl6*, *Psat1*, *Ank* (**b**), *Fn1* (**c**), *Spp1* (**e**), *Cybb* (**g**), *H2-Aa* and *H2-Ab1* (**i**), *Ccl4* (**j**) transcripts after cuprizone challenge. Genes shown in (**a**) were upregulated in both de-and remyelination, whereas genes depicted in (**b, c, e**) or (**g, i**) were increased in demyelination-associated cluster Adt-C5, C6, or in the remyelination- associated Adt-C7, C8, respectively. Color keys represent the respective expression levels. (**d**) Left and middle panels: single-molecule fluorescent *in situ* hybridization (smFISH) for *Fn1* and *Cx3cr1* reveals subpopulations of microglia after 5-week cuprizone treatment in the corpus callosum. "1" indicates *Fn1*$^{+}$*Cx3cr1*$^{+}$ microglia (yellow arrowheads: *Fn1* mRNA). "2" indicates *Fn1*$^{-}$*Cx3cr1*$^{+}$ microglia. Scale bar: 10 µm (overviews) or 3 µm (inserts). Representative pictures out of three investigated mice are shown. Blank arrowheads in the picture of control mice indicate non-specific signals. Right panel: percentage of *Fn1*$^{+}$ *Cx3cr1*$^{+}$ microglia in the corpus callosum. Bar represents mean ± SEM of three animals (168 investigated cells). (**e**) *Spp1* mRNA expression after cuprizone challenge. Expression of *Spp1* is found to be upregulated in Adt-C5 and C6. The color key indicates the expression levels. (**f**) Left and middle panels: smFISH for *Spp1* and *Cx3cr1* reveals subpopulations of microglia after 5-week cuprizone treatment in the corpus callosum. "1" indicates *Spp1*$^{+}$*Cx3cr1*$^{+}$ microglia (yellow arrowheads: *Spp1* mRNA). "2" indicates *Spp1*$^{-}$ *Cx3cr1*$^{+}$ microglia. Scale bars: 10 µm (overviews) and 3 µm (inserts). Representative pictures out of three investigated mice are shown. Right panel: percentage of *Spp1*$^{+}$*Cx3cr1*$^{+}$ microglia in the corpus callosum. Bar represents mean ± SEM of three animals (165 investigated cells). (**g**) *t*-SNE plot depicting *Spp1* expression after cuprizone challenge. The color key indicates the expression levels (**h**) Left and middle panels: smFISH for *Cybb* and *Cx3cr1* reveals subpopulations of microglia after 5 weeks cuprizone treatment in the corpus callosum. "1" indicates *Cybb*$^{+}$*Cx3cr1*$^{+}$ microglia (yellow arrowheads: *Cybb* mRNA). "2" indicates *Cybb*$^{-}$ *Cx3cr1*$^{+}$ microglia. Scale bars: 10 µm (overviews) and 3 µm (inserts). Representative pictures out of three investigated mice are shown. Right panel: percentage of *Cybb*$^{+}$*Cx3cr1*$^{+}$ microglia in the corpus callosum. Bar represents mean ± SEM of three animals (165 investigated cells). The color key represents the expression levels.

Extended Data Figure 5: Microglial subtypes in healthy human brains.

(a) *t*-SNE plot of 1180 human microglia showing the distribution of individual microglia from five patients. Each dot represents a single cell. Different colors indicate different patients,

(b) Heat map showing the distribution of the healthy human clusters (HHu-C) in each individual patient.

(c) *t*-SNE plot showing the expression of *P2RY13*. Each dot represents a single cell. Color codes represent expression levels.

Extended Data Figure 6: Detailed neuropathological characterization of human MS lesions.

Histology of the MS brains (MS-1 patient until MS-5 patient) using hematoxylin and eosin (H&E), luxol fast blue (LFB-PAS), 2',3'-cyclic-nucleotide 3'-phosphodiesterase (CNPase), and myelin basic protein (MBP) for myelin, human leukocyte antigen – DR isotype (HLA-DR) and CD68 for myeloid cells, CD3 for T cells, CD20 for B cells and Bielschowsky (Biel) for axons. Scale bar: 50 µm. Lesions are typical early active MS lesions according to the standard classification system (*50*).

Extended Data Figure 7: Molecular profile of microglia subsets during MS.

(a-e) *t*-SNE plots of genes enriched in cluster Hu-C5-7 (**a**), Hu-C2 (**b**), Hu-C3 (**c**), Hu-C4 (**d**), Hu-C8 (**e**) are shown. Color codes represent expression levels.

(f) *t*-SNE plots depicting genes upregulated in the clusters Hu-C2, Hu-C3 and Hu-C8. Color codes represent expression levels.

(g) *t*-SNE plots of genes that were upregulated in the disease-associated microglia subsets in the mouse demyelination model, but not in the microglia in the MS patient brains. Color codes represent expression levels.

Extended Data Figure 8: Pairwise correlation analysis of scRNA-seq data from mouse and human microglia.

(a) Canonical correlation analysis (Seurat alignment procedure) visualizing shared correlation structures (i.e., canonical correlation vectors, CC) between mouse and human data sets. Each dot represents single cell.

(b) CC Plot of cells assigned as mouse C7-C13 and human Hu-C1-C10. Mouse demyelination-related microglia clusters (C12 and C13) are transcriptionally close to human MS-associated microglia clusters (Hu-C2, Hu-C3 and Hu-C8). Each dot represents single cell.

(c) Violin plots depicting a shared gene correlation structure that is conserved between mouse and human clusters.

Extended Data Figure 9: Graphical abstract of experimental findings.

SUPPLEMENTAL FIGURES AND TABLE

Supplementary Figure 1: FACS gating strategy for microglia isolation.
CNS cells were gated for G1 and G2 (singlets), followed by being gated for living cell (G3, fixable viability dye), $CD45^{int}CD11b^{+}$ (G4), $Ly6C^{-}Ly6G^{-}$ (G5), and $CD206^{-}$ (G6).

Supplementary Figure 2: related to figure 2-5
t-SNE plots depicting single microglia from the replicates from different CNS regions of individual embryos, juvenile and adult mice and diseased mice.

Supplementary Figure 3: related to figure 3
Heat map of all differentially regulated genes that were up- or down-regulated in each cluster microglia during development.

Supplementary Figure 4: related to figure 5
Heat map of all differentially regulated genes that were up- or down-regulated in each cluster.

Supplementary Figure 5: related to figure 6
Heat map of top 68 differentially regulated genes that were up- or down-regulated in each cluster of healthy human microglia.

Supplementary Figure 6: related to figure 6
Heat map of top 148 differentially regulated genes that were up- or down-regulated in each cluster of both healthy and MS-patient microglia.

Supplementary Table 1:
Sheet 1: Information on mice and cells used in each scRNA-seq analysis including genotype, strain, sex, condition, age, CNS region and cell numbers.
Sheet 2: Details on patients and cells used in each scRNAseq analysis including sex, condition, age, CNS region and cell numbers.

Reference List

1. R. M. Ransohoff, V. H. Perry, *Annu. Rev Immunol.* **27**, 119 (2009).
2. M. Colonna, O. Butovsky, *Annu. Rev. Immunol.* **35**, 441 (2017).
3. J. Herz, A. J. Filiano, A. Smith, N. Yogev, J. Kipnis, *Immunity.* **46**, 943 (2017).
4. M. Prinz, D. Erny, N. Hagemeyer, *Nat. Immunol.* **18**, 385 (2017).
5. F. Ginhoux, S. Jung, *Nat. Rev. Immunol.* **14**, 392 (2014).
6. C. Schulz *et al.*, *Science* **336**, 86 (2012).
7. K. Kierdorf *et al.*, *Nat. Neurosci* **16**, 273 (2013).
8. T. Goldmann *et al.*, *Nat. Immunol.* **17**, 797 (2016).
9. K. Molawi *et al.*, *J. Exp. Med.* **211**, 2151 (2014).
10. N. Mossadegh-Keller *et al.*, *J. Exp. Med.* **214**, 2829 (2017).
11. S. Ensan *et al.*, *Nat. Immunol.* (2015).
12. N. Hagemeyer *et al.*, *Acta Neuropathol.* (2017).
13. T. L. Tay *et al.*, *Nat. Neurosci.* **20**, 793 (2017).
14. P. Fuger *et al.*, *Nat. Neurosci.* **20**, 1371 (2017).
15. K. Askew *et al.*, *Cell Rep.* **18**, 391 (2017).
16. A. C. Wendeln *et al.*, *Nature* **556**, 332 (2018).
17. D. Erny *et al.*, *Nat. Neurosci.* **18**, 965 (2015).
18. J. Bruttger *et al.*, *Immunity.* **43**, 92 (2015).
19. S. E. Hickman *et al.*, *Nat. Neurosci.* (2013).
20. K. J. Doorn *et al.*, *Front Cell Neurosci.* **9**, 84 (2015).
21. K. Grabert *et al.*, *Nat. Neurosci.* **19**, 504 (2016).
22. K. Sharma *et al.*, *Nat. Neurosci.* **18**, 1819 (2015).
23. K. Kierdorf, N. Katzmarski, C. A. Haas, M. Prinz, *PLoS. One.* **8**, e58544 (2013).
24. A. Wlodarczyk *et al.*, *EMBO J.* (2017).
25. O. Matcovitch-Natan *et al.*, *Science* **353**, aad8670 (2016).
26. T. Goldmann *et al.*, *EMBO J.* **34**, 1612 (2015).
27. S. Krasemann *et al.*, *Immunity.* **47**, 566 (2017).

28. M. J. T. Stubbington, O. Rozenblatt-Rosen, A. Regev, S. A. Teichmann, *Science* **358**, 58 (2017).

29. D. Gosselin *et al.*, *Science* **356**, (2017).

30. T. F. Galatro, I. D. Vainchtein, N. Brouwer, E. W. G. M. Boddeke, B. J. L. Eggen, *Methods Mol. Biol.* **1559**, 333 (2017).

31. Y. Lavin *et al.*, *Cell* **159**, 1312 (2014).

32. H. Mathys *et al.*, *Cell Rep.* **21**, 366 (2017).

33. H. Keren-Shaul *et al.*, *Cell* **169**, 1276 (2017).

34. A. Zeisel *et al.*, *Science* **347**, 1138 (2015).

35. D. Grun *et al.*, *Cell Stem Cell* **19**, 266 (2016).

36. M. Prinz, J. Priller, *Nat. Rev. Neurosci.* **15**, 300 (2014).

37. A. Mildner *et al.*, *Nat. Neurosci.* **10**, 1544 (2007).

38. E. N. Benveniste, *J. Mol. Med. (Berl)* **75**, 165 (1997).

39. W. Bruck *et al.*, *Ann. Neurol.* **38**, 788 (1995).

40. O. Butovsky *et al.*, *Nat. Neurosci.* **17**, 131 (2014).

41. L. J. Lawson, V. H. Perry, S. Gordon, *Neuroscience* **48**, 405 (1992).

42. Y. Wang *et al.*, *Nat. Immunol.* **13**, 753 (2012).

43. L. M. De Biase *et al.*, *Neuron* **95**, 341 (2017).

44. T. Zrzavy *et al.*, *Brain* **140**, 1900 (2017).

45. A. Mildner, H. Huang, J. Radke, W. Stenzel, J. Priller, *Glia* **65**, 375 (2017).

46. T. Hashimshony *et al.*, *Genome Biol.* **17**, 77 (2016).

47. H. Li, R. Durbin, *Bioinformatics.* **26**, 589 (2010).

48. D. Grun, L. Kester, O. A. van, *Nat. Methods* **11**, 637 (2014).

49. J. Raasch *et al.*, *Brain* **134**, 1184 (2011).

50. C. Lucchinetti *et al.*, *Ann. Neurol.* **47**, 707 (2000).

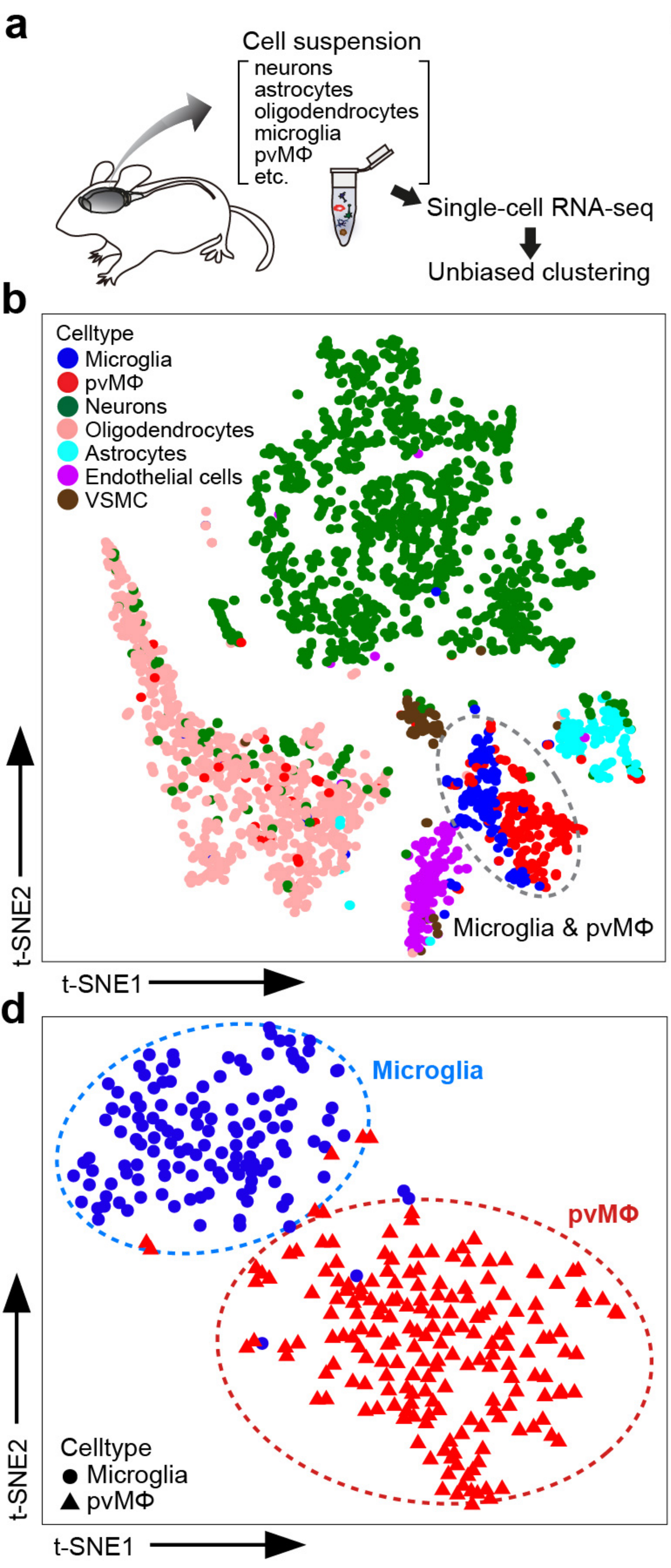
a
Cell suspension
neurons
astrocytes
oligodendrocytes
microglia
pvMΦ
etc.
Single-cell RNA-seq
Unbiased clustering
b
Celltype
Microglia
pvMΦ
Neurons
Oligodendrocytes
Astrocytes
Endothelial cells
VSMC
Microglia & pvMΦ
t-SNE2
t-SNE1
d
Microglia
pvMΦ
Celltype
Microglia
pvMΦ
t-SNE2
t-SNE1
c
z−score
−2 0 2
Astrocytes
Endothelial cells
Microglia
Neurons
Oligodendrocytes
pvMΦ
VSMC
Fabp7
Aqp4
Gfap
Aldoc
Acsbg1
Ntsr2
Aldh1l1
Slc38a5
Ctla2a
Slc7a5
Pecam1
Cldn5
Icam2
Hexb
Gpr34
P2ry12
Siglech
Tgfbr1
Ccr5
Tmem119
Selplg
Il1a
Thy1
Syn1
Crym
Cpne6
Slc17a7
Spink8
Plp1
Mbp
Mog
Mobp
Ugt8a
Opalin
Cd209f
Ccl24
Cd163
Pf4
Mrc1
Cbr2
F13a1
Lyve1
Folr2
Myh11
Acta2
Myl9
Tpm2
Mustn1
Crispld2

Figure 1

a

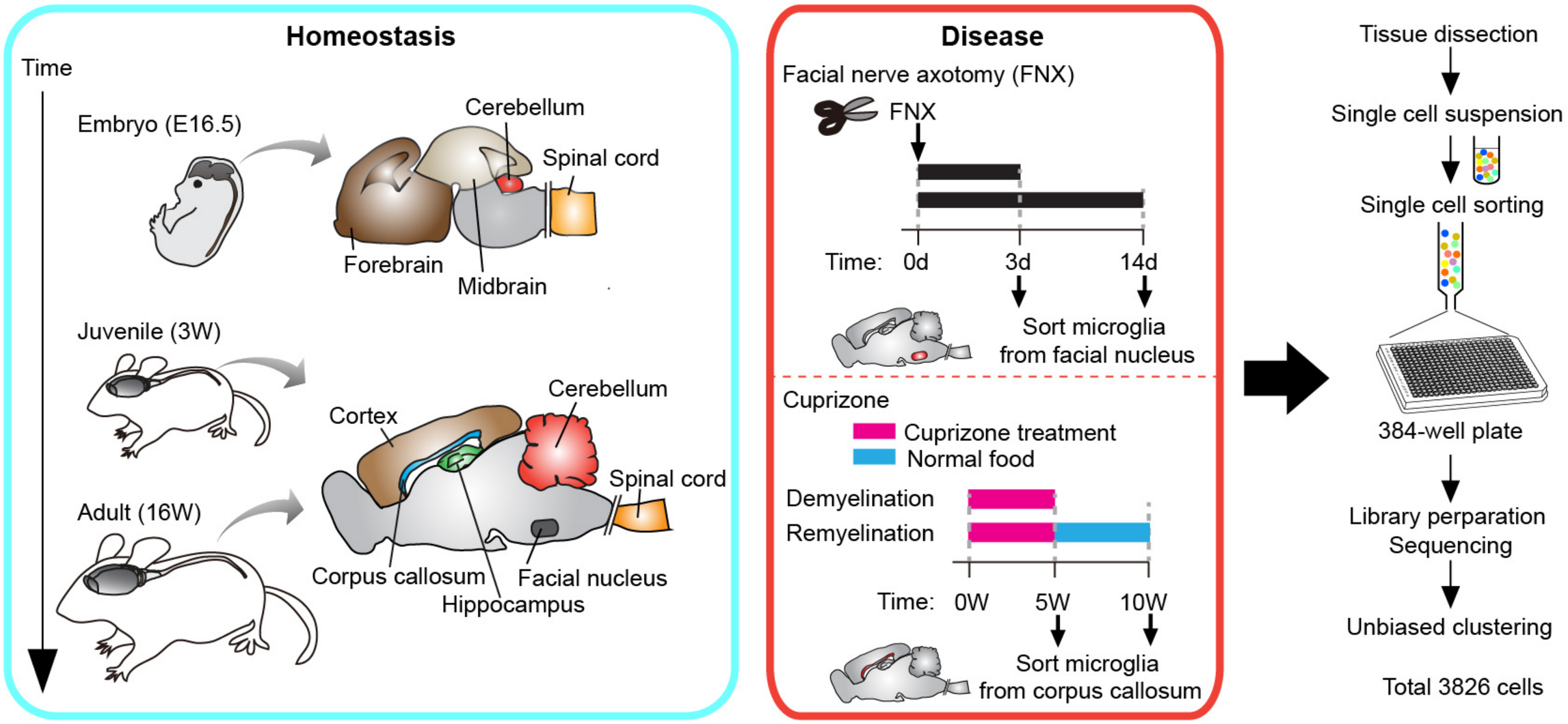
Homeostasis
Time
Embryo (E16.5)
Cerebellum
Spinal cord
Forebrain
Midbrain
Juvenile (3W)
Cerebellum
Cortex
Spinal cord
Adult (16W)
Corpus callosum
Facial nucleus
Hippocampus
Disease
Facial nerve axotomy (FNX)
FNX
Time: 0d 3d 14d
Sort microglia
from facial nucleus
Cuprizone
Cuprizone treatment
Normal food
Demyelination
Remyelination
Time: 0W 5W 10W
Sort microglia
from corpus callosum
Tissue dissection
Single cell suspension
Single cell sorting
384-well plate
Library perparation
Sequencing
Unbiased clustering
Total 3826 cells

b

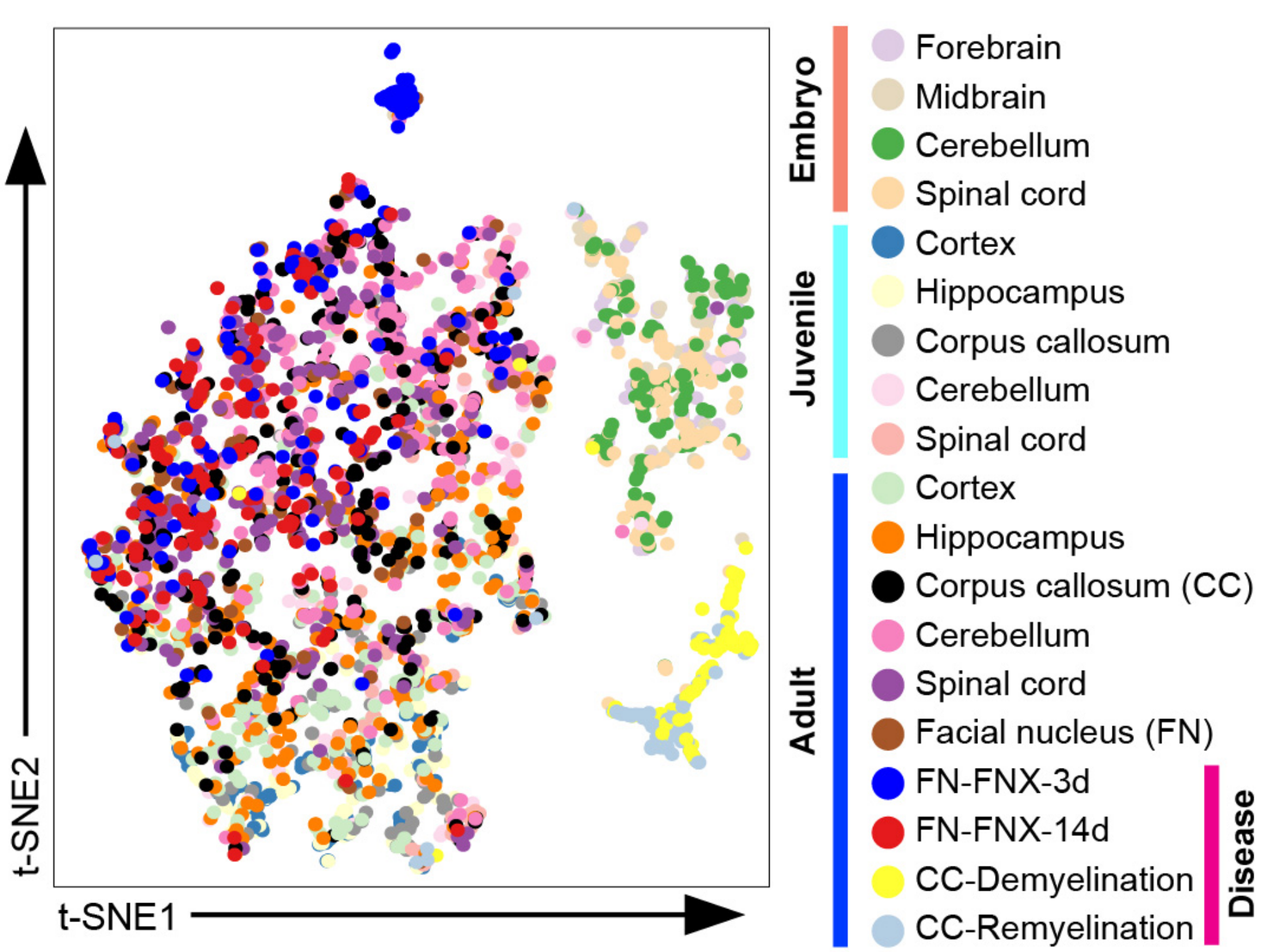
t-SNE2
t-SNE1
Embryo
Juvenile
Adult
Disease
Forebrain
Midbrain
Cerebellum
Spinal cord
Cortex
Hippocampus
Corpus callosum
Cerebellum
Spinal cord
Cortex
Hippocampus
Corpus callosum (CC)
Cerebellum
Spinal cord
Facial nucleus (FN)
FN-FNX-3d
FN-FNX-14d
CC-Demyelination
CC-Remyelination

c

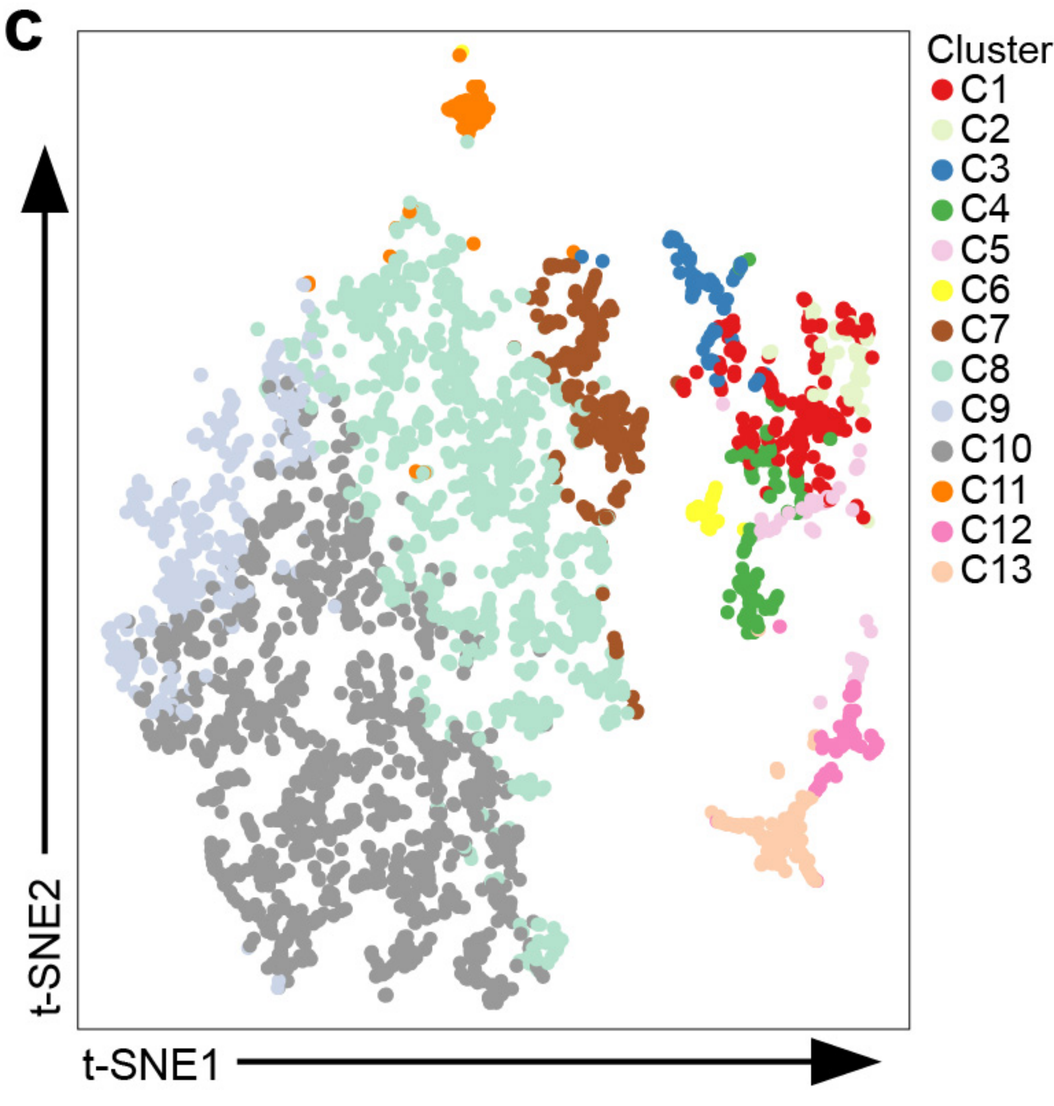
t-SNE2
t-SNE1
Cluster
C1
C2
C3
C4
C5
C6
C7
C8
C9
C10
C11
C12
C13

Figure 2

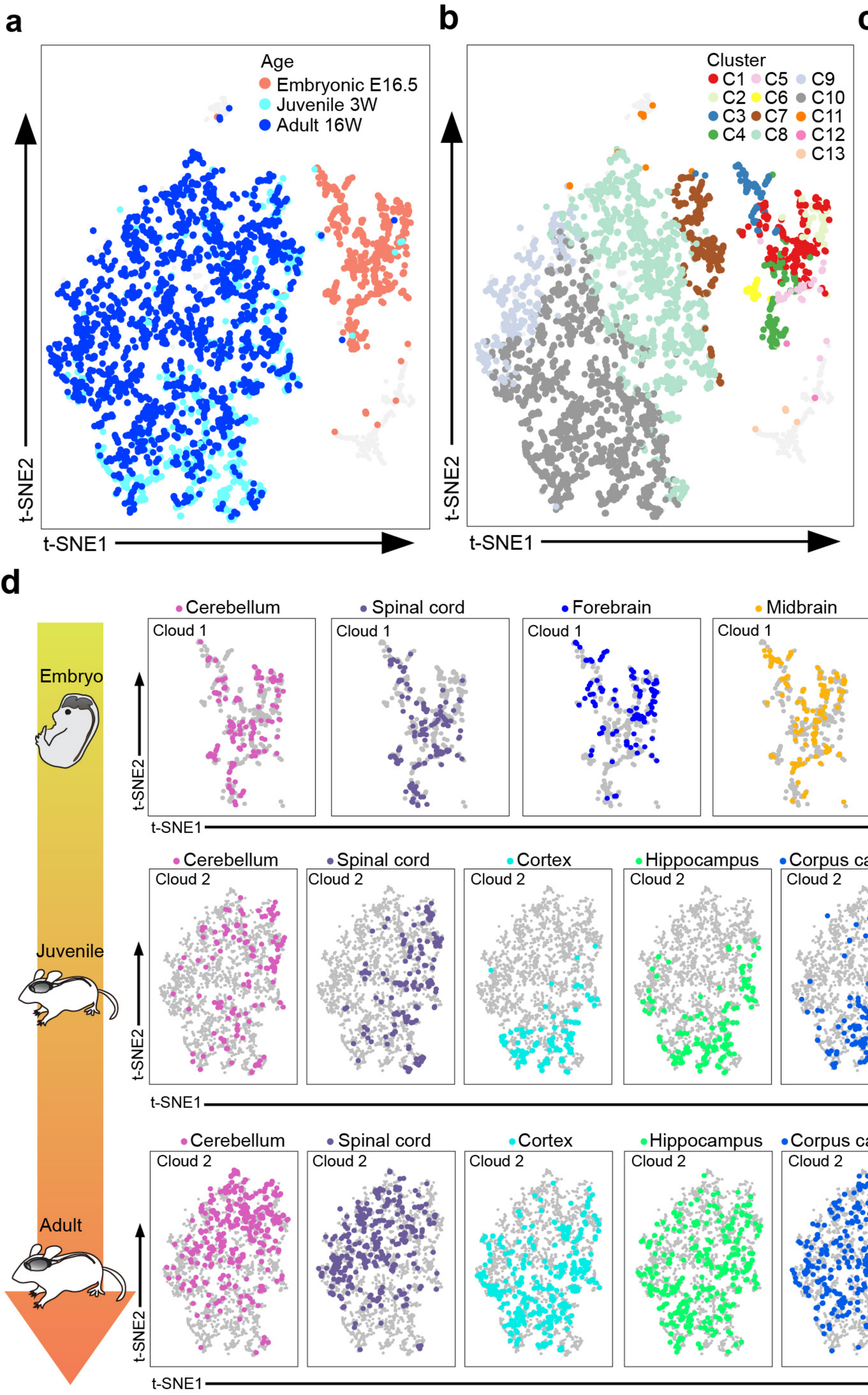
a
Age
Embryonic E16.5
Juvenile 3W
Adult 16W
t-SNE2
t-SNE1
b
Cluster
C1 C2 C3 C4 C5 C6 C7 C8 C9 C10 C11 C12 C13
t-SNE2
t-SNE1
c
Cluster
C1 C2 C3 C4 C5 C6 C7 C8 C9 C10 C11 C12 C13
z-score
-2 0 2 4
Ctsb
Malat1
Apoe
Sparc
Tmsb4x
Selplg
Cst3
Tmem119
Rpl4
Eef1a1
d
Embryo
Juvenile
Adult
Cerebellum
Spinal cord
Forebrain
Midbrain
Cloud 1
t-SNE2
t-SNE1
Age
Embryonic E16.5
Juvenile 3W
Adult 16W
Cloud 2
Cloud 1
Cerebellum
Spinal cord
Cortex
Hippocampus
Corpus callosum
Facial nucleus
Cloud 2
t-SNE2
t-SNE1
e
Proportion (%)
Cerebellum
Spinal cord
Forebrain
Midbrain
Cortex
Hippocampus
Corpus callosum
Facial nucleus
Cluster
C1 C2 C3 C4 C5 C6 C7 C8 C9 C10 C11 C12 C13

Figure 3

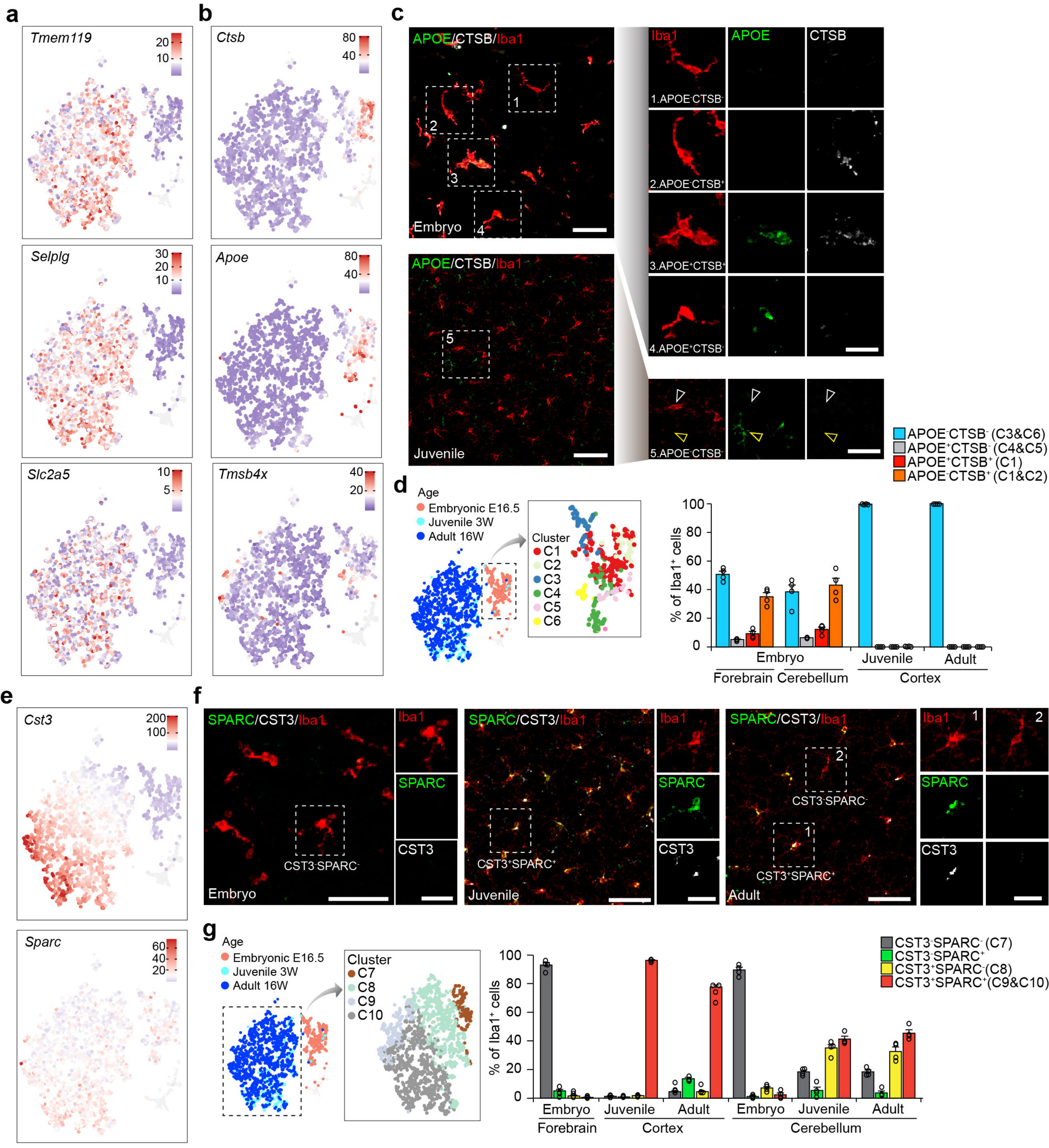
a
Tmem119
20
10
Ctsb
80
40
Selplg
30
20
10
Apoe
80
40
Slc2a5
10
5
Tmsb4x
40
20
b
c
APOE/CTSB/Iba1
1
2
3
4
Embryo
APOE/CTSB/Iba1
5
Juvenile
Iba1
APOE
CTSB
1.APOE-CTSB-
2.APOE-CTSB+
3.APOE+CTSB+
4.APOE+CTSB-
5.APOE-CTSB-
APOE-CTSB- (C3&C6)
APOE+CTSB- (C4&C5)
APOE+CTSB+ (C1)
APOE-CTSB+ (C1&C2)
d
Age
Embryonic E16.5
Juvenile 3W
Adult 16W
Cluster
C1
C2
C3
C4
C5
C6
% of Iba1+ cells
100
80
60
40
20
0
Embryo
Juvenile
Adult
Forebrain
Cerebellum
Cortex
e
Cst3
200
100
Sparc
60
40
20
f
SPARC/CST3/Iba1
Iba1
SPARC
CST3
CST3-SPARC-
Embryo
CST3+SPARC+
Juvenile
2
1
Adult
g
Age
Embryonic E16.5
Juvenile 3W
Adult 16W
Cluster
C7
C8
C9
C10
CST3-SPARC- (C7)
CST3-SPARC+
CST3+SPARC-(C8)
CST3+SPARC+(C9&C10)
Forebrain
Cortex
Cerebellum

Figure 4

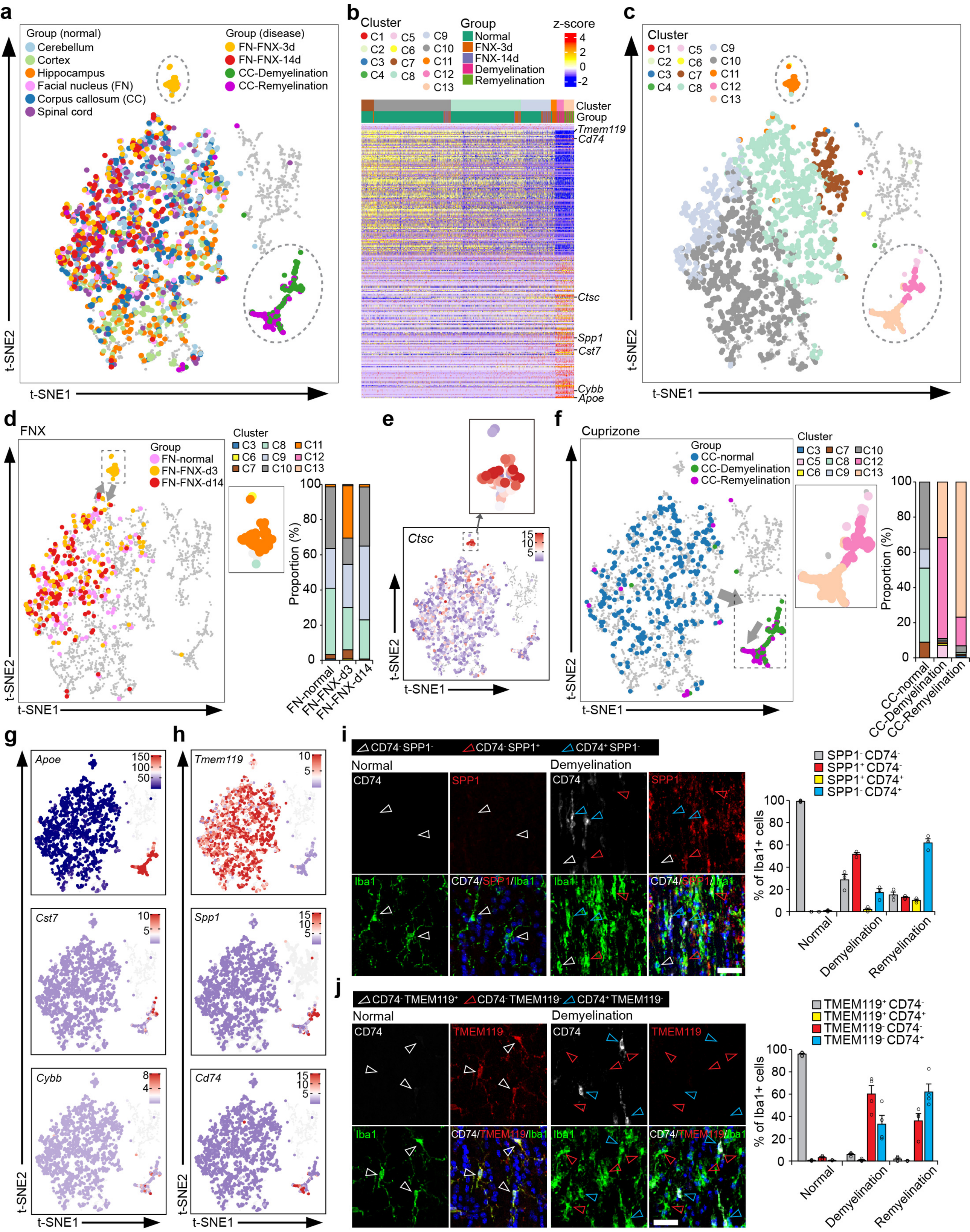
a
Group (normal)
Cerebellum
Cortex
Hippocampus
Facial nucleus (FN)
Corpus callosum (CC)
Spinal cord
Group (disease)
FN-FNX-3d
FN-FNX-14d
CC-Demyelination
CC-Remyelination
t-SNE1
t-SNE2
b
Cluster
C1 C2 C3 C4 C5 C6 C7 C8 C9 C10 C11 C12 C13
Group
Normal
FNX-3d
FNX-14d
Demyelination
Remyelination
z-score
4
2
0
-2
Cluster
Group
Tmem119
Cd74
Ctsc
Spp1
Cst7
Cybb
Apoe
c
Cluster
C1 C2 C3 C4 C5 C6 C7 C8 C9 C10 C11 C12 C13
t-SNE1
t-SNE2
d
FNX
Group
FN-normal
FN-FNX-d3
FN-FNX-d14
Cluster
C3 C8 C11 C6 C9 C12 C7 C10 C13
Proportion (%)
FN-normal
FN-FNX-d3
FN-FNX-d14
t-SNE1
t-SNE2
e
Ctsc
15
10
5
t-SNE1
t-SNE2
f
Cuprizone
Group
CC-normal
CC-Demyelination
CC-Remyelination
Cluster
C3 C7 C10 C5 C8 C12 C6 C9 C13
Proportion (%)
CC-normal
CC-Demyelination
CC-Remyelination
t-SNE1
t-SNE2
g
Apoe
150
100
50
Cst7
10
5
Cybb
8
4
t-SNE1
t-SNE2
h
Tmem119
10
5
Spp1
15
10
5
Cd74
15
10
5
t-SNE1
t-SNE2
i
CD74- SPP1-
CD74- SPP1+
CD74+ SPP1-
Normal
Demyelination
CD74
SPP1
Iba1
CD74/SPP1/Iba1
SPP1- CD74-
SPP1+ CD74-
SPP1+ CD74+
SPP1- CD74+
% of Iba1+ cells
Normal
Demyelination
Remyelination
j
CD74- TMEM119+
CD74- TMEM119-
CD74+ TMEM119-
Normal
Demyelination
CD74
TMEM119
Iba1
CD74/TMEM119/Iba1
TMEM119+ CD74-
TMEM119+ CD74+
TMEM119- CD74-
TMEM119- CD74+
% of Iba1+ cells
Normal
Demyelination
Remyelination

Figure 5

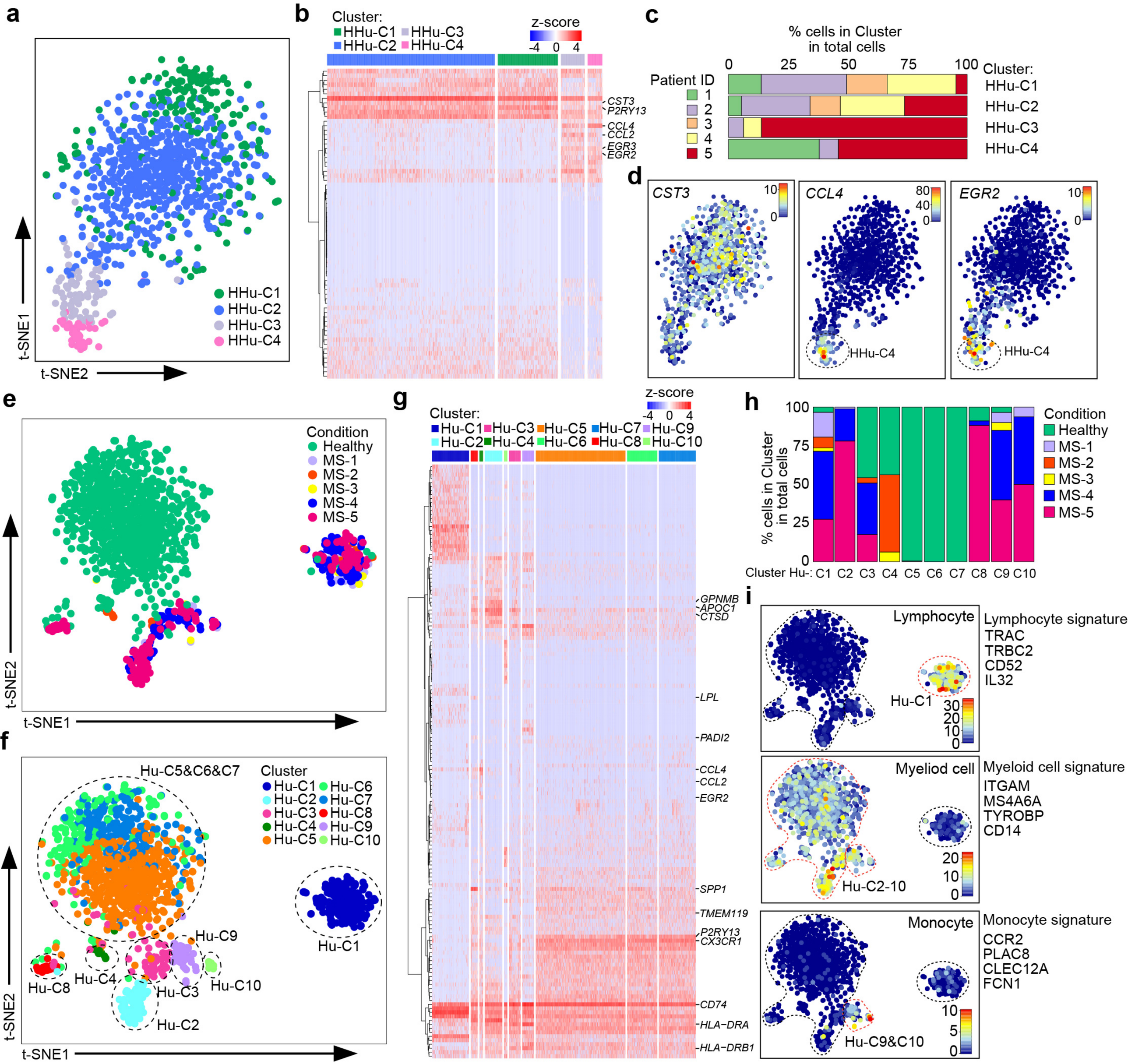
a
t-SNE1
t-SNE2
HHu-C1
HHu-C2
HHu-C3
HHu-C4
b
Cluster:
HHu-C1
HHu-C2
HHu-C3
HHu-C4
z-score
-4 0 4
CST3
P2RY13
CCL4
CCL2
EGR3
EGR2
c
% cells in Cluster
in total cells
0 25 50 75 100
Patient ID
1
2
3
4
5
Cluster:
HHu-C1
HHu-C2
HHu-C3
HHu-C4
d
CST3
10
0
CCL4
80
40
0
HHu-C4
EGR2
10
0
HHu-C4
e
Condition
Healthy
MS-1
MS-2
MS-3
MS-4
MS-5
t-SNE1
t-SNE2
f
Hu-C5&C6&C7
Cluster
Hu-C1
Hu-C2
Hu-C3
Hu-C4
Hu-C5
Hu-C6
Hu-C7
Hu-C8
Hu-C9
Hu-C10
Hu-C1
Hu-C9
Hu-C8
Hu-C4
Hu-C3
Hu-C10
Hu-C2
t-SNE1
t-SNE2
g
z-score
-4 0 4
Cluster:
Hu-C1
Hu-C2
Hu-C3
Hu-C4
Hu-C5
Hu-C6
Hu-C7
Hu-C8
Hu-C9
Hu-C10
GPNMB
APOC1
CTSD
LPL
PADI2
CCL4
CCL2
EGR2
SPP1
TMEM119
P2RY13
CX3CR1
CD74
HLA-DRA
HLA-DRB1
h
% cells in Cluster
in total cells
100
75
50
25
0
Cluster Hu-: C1 C2 C3 C4 C5 C6 C7 C8 C9 C10
Condition
Healthy
MS-1
MS-2
MS-3
MS-4
MS-5
i
Lymphocyte
Hu-C1
30
20
10
0
Lymphocyte signature
TRAC
TRBC2
CD52
IL32
Myeliod cell
Hu-C2-10
20
10
0
Myeloid cell signature
ITGAM
MS4A6A
TYROBP
CD14
Monocyte
Hu-C9&C10
10
5
0
Monocyte signature
CCR2
PLAC8
CLEC12A
FCN1

Figure 6

j

Homeostatic Hu-C5,6,7

Enriched genes
TMEM119
P2RY13
CX3CR1
SLC2A5
P2RY12

TMEM119

MS-associated Hu-C2

Enriched genes	Microglial genes
CTSD	*TMEM119*$^{-}$
APOC1	*P2RY13*^{lo}
GPNMB	*CX3CR1*$^{-}$
ANXA2	*SLC2A5*^{lo}
LGALS1	*P2RY12*$^{-}$

CTSD

Hu-C2

MS-enriched Hu-C8

Enriched genes	Microglial genes
SPP1	*TMEM119*^{lo}
PADI2	*P2RY13*^{lo}
LPL	*CX3CR1*^{lo}
CPM	*SLC2A5*^{lo}
LIPA	*P2RY12*$^{-}$

SPP1

Hu-C8

Homeostatic Hu-C4

Enriched genes	Microglial genes
CCL4	*TMEM119*^{lo}
EGR2	*P2RY13*^{lo}
CCL2	*CX3CR1*^{lo}
EGR3	*SLC2A5*^{lo}
CD83	*P2RY12*^{lo}

CCL4

Hu-C4

MS-enriched Hu-C3

Enriched genes	Microglial genes
CD74	*TMEM119*$^{-}$
HLA-DRA	*P2RY13*^{lo}
HLA-DRB1	*CX3CR1*^{lo}
HLA-DPB1	*SLC2A5*$^{-}$
LYZ	*P2RY12*$^{-}$

CD74

Hu-C3

l

Healthy MS

MRP14/Iba1/DAPI

1 MRP14^{-}

2 MRP14^{+}

■ microglia (MRP14^{-})
□ monocyte (MRP14^{+})

% of Iba1+ cells

Healthy MS

k

Healthy MS

TMEM119 Iba1 TMEM119/Iba1/DAPI

m

Healthy MS

SPP1/ CTSD/ Iba1/ MRP14

SPP1^{-}CTSD^{-}

SPP1^{+}CTSD^{-}

SPP1^{-}CTSD^{+}

SPP1^{+}CTSD^{+}

Healthy-1 Healthy-2 Healthy-3 Healthy-4

MS-1 MS-2 MS-3 MS-5

n

Healthy MS

SPP1/ CD74/ Iba1/ MRP14

SPP1^{-}CD74^{-}

SPP1^{+}CD74^{-}

SPP1^{-}CD74^{+}

SPP1^{+}CD74^{+}

Healthy-1 Healthy-2 Healthy-3 Healthy-4

MS-1 MS-2 MS-3 MS-5

Mouse Normal

Demyelination

Remyelination

Figure 6